

Amyloid-like aggregates cause lysosomal defects in neurons via gain-of-function toxicity

Tillman Schaefer^{1,9,*}, Irene Riera-Tur^{2,*}, Daniel Hornburg^{3,4,10,*}, Archana Mishra^{2,*}, Lorena Fernández-Mosquera⁵, Nuno Raimundo⁵, Matthias Mann³, Wolfgang Baumeister¹, Rüdiger Klein², Felix Meissner⁴, Rubén Fernández-Busnadiego^{1,6,7,#} and Irina Dudanova^{2,8,#}

¹Department of Molecular Structural Biology, Max Planck Institute of Biochemistry, Martinsried, Germany

²Department of Molecules – Signaling – Development, Max Planck Institute of Neurobiology, Martinsried, Germany

³Department of Proteomics and Signal Transduction, Max Planck Institute of Biochemistry, Martinsried, Germany

⁴Experimental Systems Immunology Group, Max Planck Institute of Biochemistry, Martinsried, Germany

⁵Institute of Cellular Biochemistry, University Medical Center Goettingen, Goettingen, Germany

⁶Institute of Neuropathology, University Medical Center Goettingen, Goettingen, Germany

⁷Cluster of Excellence "Multiscale Bioimaging: from Molecular Machines to Networks of Excitable Cells" (MBExC), University of Goettingen, Goettingen, Germany

⁸Molecular Neurodegeneration Group, Max Planck Institute of Neurobiology, Martinsried, Germany

⁹Current affiliation: Cryo-EM Facility, Max Planck Institute of Biochemistry, Martinsried, Germany

¹⁰Current affiliation: Department of Genetics, Stanford University School of Medicine, Stanford, CA, USA

*These authors contributed equally

#These authors contributed equally

Correspondence:

ruben.fernandezbusnadiego@med.uni-goettingen.de (R.F.-B.), idudanova@neuro.mpg.de (I.D.)

Keywords: protein aggregation, neurodegeneration, autophagy-lysosomal pathway, cryo-electron tomography, mass spectrometry

Abstract

The autophagy-lysosomal pathway is impaired in many neurodegenerative diseases characterized by protein aggregation, but the link between aggregation and lysosomal dysfunction remains poorly understood. Here, we use artificial amyloid-like β -sheet proteins (β proteins) to investigate the gain-of-function effects of protein aggregation in primary neurons. We show that β proteins form fibrillar aggregates and cause neurotoxicity. Cryo-electron tomography reveals lysosomal alterations reminiscent of lysosomal storage disorders. Mass spectrometry-based analysis of the β protein interactome shows that β proteins sequester AP-3 μ 1, a subunit of the AP-3 adaptor complex involved in protein trafficking to lysosomal organelles. Importantly, restoring AP-3 μ 1 expression ameliorates neurotoxicity caused by β proteins. Our results point to lysosomes as particularly vulnerable organelles in neurodegenerative diseases, and emphasize the role of toxic gain-of-function of protein aggregates in lysosomal defects.

Introduction

The autophagy-lysosomal system is a major cellular degradation pathway for long-lived proteins, macromolecular complexes and damaged organelles (Finkbeiner, 2019; Settembre et al., 2013). Defects in this system cause a number of severe disorders known as lysosomal storage diseases, often characterized by early-onset neurodegeneration (Fraldi et al., 2016; Platt et al., 2018). In addition, lysosomal function is compromised in many age-related neurodegenerative disorders, such as amyotrophic lateral sclerosis, Alzheimer's, Parkinson's and Huntington's disease (Abeliovich and Gitler, 2016; Finkbeiner, 2019; Fraldi et al., 2016; Taylor et al., 2016; Wang et al., 2018). Another convergent feature of late-onset neurodegenerative diseases is protein misfolding and aggregation, which leads to accumulation of toxic protein species and neuronal demise (Soto and Pritzkow, 2018). As autophagy represents an important pathway for removal of aggregated proteins, dysfunction of the autophagy-lysosomal system facilitates the build-up of aggregates (Finkbeiner, 2019; Wang et al., 2018). Conversely, aggregating proteins themselves might directly interfere with the normal function of the autophagy-lysosomal machinery, as has been shown for mutant Huntingtin (Wong and Holzbaur, 2014) and alpha-synuclein (Cuervo et al., 2004; Winslow et al., 2010). In spite of these insights into the interactions of aggregating proteins with the autophagy-lysosomal pathway, the mechanistic link between aggregate formation and lysosomal impairments is not completely understood. Moreover, it remains unclear whether autophagy-lysosomal impairment occurs prior to accumulation of aggregates within this degradation pathway or is a consequence of this phenomenon.

One difficulty in studying the role of protein aggregation in cellular dysfunction is the overlap of gain- and loss-of function effects resulting from protein misfolding. On the one hand, reduction in the cellular pool of the correctly folded form of the protein results in a partial loss of its native function. At the same time, the misfolded conformation of the protein can engage in aberrant interactions with cellular membranes and with other proteins, causing gain-of-function toxicity (Bauerlein et al., 2017; Chiti and Dobson, 2017; Kim et al., 2016; Olzscha et al., 2011; Winner et al., 2011; Yang and Hu, 2016). Such loss- and gain-of-function phenomena occur in parallel and are difficult to disentangle, especially since the native functions of many aggregating proteins are still poorly understood (Brothers et al., 2018; Saudou and Humbert, 2016; Winklhofer et al., 2008). To overcome this challenge, here we take advantage of artificial proteins (hereafter β proteins), which have been

rationally designed to form antiparallel β -sheets due to an alternating pattern of polar and non-polar amino acid residues (West et al., 1999). Antiparallel β -sheet structure is an important general property of natural aggregating proteins, as demonstrated for A β , polyQ-containing proteins, pathological tau and α -synuclein (Chiti and Dobson, 2017; Hartl, 2017). β proteins spontaneously assemble into amyloid-like fibrils *in vitro* (West et al., 1999). When expressed in cells, β proteins form intracellular inclusions and compromise cellular viability (Frottin et al., 2019; Olzscha et al., 2011; Vincenz-Donnelly et al., 2018; Woerner et al., 2016). Importantly, while being structurally similar to natural amyloids, β proteins do not possess any biological function, and therefore provide an excellent tool to specifically investigate toxic gain-of-function effects of aggregation in the absence of any loss-of-function phenomena.

In this study, we use a combination of last-generation cryo-electron tomography (cryo-ET), state-of-the-art proteomics, and cell-biological approaches to study the impact of β proteins on primary mouse neurons. We find that β protein aggregation induces neurotoxicity and leads to accumulation of enlarged, cargo-rich lysosomes. Our data suggest that these defects are mediated by the sequestration of a component of the AP-3 adaptor complex within the aggregates. Taken together, our findings point to toxic gain-of-function of protein aggregates as an important cause of lysosomal malfunction in neurodegenerative diseases.

Results

β protein aggregation causes toxicity in primary neurons

To investigate the effects of β protein aggregation in neurons, we used two β proteins (West et al., 1999), β 4 and β 23, tagged with a myc epitope and fused to mCherry (β 4-mCherry and β 23-mCherry). These proteins were expressed in dissociated murine cortical cultures using transfection and lentiviral transduction. Upon transfection of β 4-mCherry and β 23-mCherry, we observed formation of abundant cytoplasmic aggregates of irregular shape, located both in the soma and in neurites (Fig. 1a-b). With lentiviral transduction, β proteins were expressed at lower levels, but in a higher fraction of cells. Both β 4-mCherry and β 23-mCherry-transduced neurons displayed multiple small cytoplasmic aggregates (Supplementary Fig. S1a). To assess whether the presence of β proteins caused toxicity in neurons, we stained transfected cultures for the apoptotic marker cleaved caspase-3 (Fig. 1c). Both β 4-mCherry and β 23-mCherry induced a significant increase in the number of cleaved caspase-3 positive cells at DIV10+3 (Fig. 1d). In transduced cultures, MTT assay revealed significant toxicity for both β proteins from DIV10+6 onwards, corresponding to appearance of abundant aggregates in the cells (Supplementary Fig. S1a-b). Expression of the control protein mCherry did not result in toxicity (Fig. 1d and Supplementary Fig. S1b). Similar expression levels of the transduced proteins were confirmed by Western blot (Supplementary Fig. S1c-d).

The presence of aggregated proteins has been shown to affect neuronal morphology (May et al., 2014). We therefore used Sholl analysis to assess the effects of β proteins on dendritic complexity. These experiments were performed on hippocampal neurons because of their uniform morphology. We observed significantly lower dendritic complexity in β 4-mCherry as well as β 23-mCherry-transfected neurons compared to mCherry-transfected control cells (Fig. 1e-f). Altogether, these data indicate that β protein aggregates induce toxicity in primary neurons, and can therefore be used as a tool to explore the effects of protein misfolding and aggregation in neuronal cells.

Ultrastructure of neuronal β protein aggregates

We employed cryo-ET to elucidate the mechanism of β protein toxicity in neurons. This technique allows investigating the structure of protein aggregates and their impact on the cellular milieu in vitrified cells in close-to-native conditions at molecular resolution (Bauerlein et al., 2017; Gruber et al.,

2018; Guo et al., 2018; Wagner et al., 2017). Primary cortical neurons were grown on electron microscopy (EM) grids, transfected with either mCherry, β 4-mCherry or β 23-mCherry, and vitrified by plunge-freezing. Cryo-correlative microscopy allowed targeting β protein aggregates for cryo-focused ion beam (cryo-FIB) milling (Rigort et al., 2012) and subsequent cryo-ET using a Volta phase plate (Danev et al., 2014) (Supplementary Fig. S2).

Analysis of cryo-electron tomograms revealed that β protein aggregates consisted of an apparently disordered network of very thin fibrils (β 4, 4.1 ± 1.6 nm; β 23, 3.6 ± 1.1 nm in diameter; $n = 30$ fibrils in both cases; unpaired t-test, n. s.) (Fig. 2). The fibrils were highly curved and branched, similar to those observed *in vitro* (Olzscha et al., 2011). The fibrillar network encapsulated additional electron-dense structures that may correspond to cellular proteins sequestered by the aggregates (Olzscha et al., 2011; Woerner et al., 2016), such as ribosomes (Fig. 2). No substantial differences were observed between neuronal aggregates of β 4-mCherry and β 23-mCherry, or between aggregates found in neurons and in HeLa cells (Fig. 2 and Supplementary Fig. S3).

β protein aggregates were often found in direct contact with cellular membranes, especially those of the endoplasmic reticulum (ER) (Fig. 2, Supplementary Fig. S3 and S4f). In some cases, ER tubes surrounded the aggregate periphery and tunnelled through its interior (Supplementary Fig. S4f), similar to previous observations for polyQ and heat-shock induced aggregates (Bauerlein et al., 2017; Gruber et al., 2018; Wagner et al., 2017). However, in contrast to polyQ fibrils in neurons (Bauerlein et al., 2017), β protein fibrils did not appear to deform cellular membranes (Supplementary Fig. S3a, c). The ER around the aggregates often engaged in membrane contact sites with mitochondria (Supplementary Fig. S3b, d), as observed for stress-induced and polyQ aggregates (Gruber et al., 2018; Zhou et al., 2014). Altogether, the morphology and cellular interactions of β protein aggregates were reminiscent of those formed by natural aggregating proteins.

β protein expression leads to defects of lysosomal morphology

Besides the presence of aggregates, the most striking ultrastructural feature of β protein-expressing neurons was the accumulation of large endo-lysosomal organelles (Fig. 3 and Supplementary Fig. S4). In control cells, a variety of endo-lysosomes was observed, including tubular early endosomes,

multivesicular bodies and autophagolysosomes containing membranous cargo (Fig. 3a-b and Supplementary Fig. S4a-c). While all those species were also found in β protein-expressing cells, large (>1 μm in diameter) cargo-loaded autophagolysosomes were dramatically enriched. No β protein aggregates were observed within these organelles in tomograms or lamella overview images (n=38 lysosomes from 10 neurons for β 4-mCherry and 31 lysosomes from 5 neurons for β 23-mCherry). Instead, autophagolysosomes often contained extensive stacks of parallel membranes and smaller vesicles, together with an electron-dense lumen suggestive of a high protein concentration (Fig. 3c-d and Supplementary Fig. S4d-f).

Consistently, light microscopy experiments with LysoTracker-loaded neurons showed that β protein expression led to an increase in lysosomal size (Fig. 4a-b). Compared to mCherry-expressing control cells, lysosomes with a diameter larger than 1 μm were ~3.5-fold more abundant in both β 4-mCherry- and β 23-mCherry-expressing cells. However, the total number of LysoTracker-positive puncta per cell was reduced by 40% in β 4-mCherry cells and by 33% in β 23-mCherry cells (Fig. 4c). In agreement with cryo-ET findings, no significant colocalization was observed between β protein aggregates and LysoTracker-positive organelles using Pearson's correlation (PC) analysis in 36 mCherry (average PC = 0.046), 39 β 4-mCherry (average PC = 0.056) and 36 β 23-mCherry (average PC = 0.049) cells. In summary, our cryo-ET and light microscopy data show that β protein aggregation leads to the accumulation of enlarged, cargo-rich autophagolysosomes, although the aggregates themselves do not build up inside these organelles. This is compatible with a scenario in which autophagic cargo is successfully delivered to lysosomes but lysosomal degradation of such cargo is defective.

To test this hypothesis, we monitored the state of the autophagic machinery in HeLa cells transfected with β 23-mCherry by Western blot analysis of early (Beclin 1, ATG5) and late (LC3-II) autophagy markers (Yamamoto and Yue, 2014). The levels of Beclin 1 and ATG5 were not significantly different in β 23-mCherry and mCherry control cells (Fig. 4d-e), suggesting that autophagosome formation was not affected. Consistently, early autophagosomes were rarely observed by cryo-ET in either control or β protein-expressing cells (Supplementary Fig. S4e). In contrast, the late autophagosomal marker LC3-II, which is itself degraded by lysosomes, was significantly increased in β 23-mCherry cells (Fig.

4d-e). These results suggest an accumulation of mature autophagosomes/autophagolysosomes, possibly due to impaired lysosomal processing (Fraldi et al., 2016).

Moreover, real-time PCR revealed that β protein expression induced an upregulation of transcripts of numerous lysosomal proteins (Sardiello et al., 2009; Settembre et al., 2011) (Fig. 4f). Transcriptional activation of lysosomal genes represents a characteristic response to conditions in which lysosomal function is compromised and lysosomal storage occurs (Sardiello et al., 2009). If the function of the autophagy-lysosomal pathway were impaired, β protein-expressing cells would be expected to show a higher sensitivity to the inhibition of this pathway (Klucken et al., 2012). We therefore treated transfected neurons with Bafilomycin A1, which blocks lysosomal acidification as well as autophagosome-lysosome fusion (Mauvezin et al., 2015). We observed a significant increase in cell death of β 23-mCherry-transfected neurons treated with 80 nM Bafilomycin, a concentration that did not significantly affect survival of mCherry control cells (Fig. 4g). Taken together, our data suggest that β protein aggregates do not affect early stages of autophagy, but impair lysosomal degradation of autophagic cargo.

Interactome of β proteins in neurons

To search for the molecular causes of lysosomal alterations in β protein-expressing neurons, we characterized the interactome of β proteins using quantitative label-free mass spectrometry (MS). In addition to β 4-mCherry and β 23-mCherry, in these experiments we also used mCherry-fused β 17, another artificial amyloid-like protein from the β protein library (Olzscha et al., 2011; West et al., 1999). Primary cortical neurons lentivirally transduced with β 4-mCherry, β 17-mCherry, β 23-mCherry or mCherry alone were harvested at DIV10+4, a time point when β proteins are still largely soluble and do not cause massive cell death (Supplementary Fig. S1a-b). Immunoprecipitation against mCherry was then performed to isolate interacting proteins. In addition, the total proteome of β protein-expressing neurons was analyzed.

We identified 30 β 4-mCherry interactors, 54 β 17-mCherry interactors and 59 β 23-mCherry interactors using highly stringent criteria (Fig. 5a-d and Supplementary Table S1). The increasing number of interactors is in line with the increasing aggregation propensity of these proteins, as observed

previously in HEK293T cells (Olzscha et al., 2011). There was an extensive overlap between the interactors of the three β proteins (Fig. 5a, e, Supplementary Table S1). In addition to confirming several interactions found previously in non-neuronal cells (Olzscha et al., 2011), our approach uncovered a number of neuron-specific interactors, including several proteins previously linked to neurodegenerative disorders (Supplementary Table S1). For example, mutations in Aimp1 cause severe infantile-onset cortical degeneration (Armstrong et al., 2014); a genetic variant of Mark4 is associated with sporadic early-onset Alzheimer's disease (Rovelet-Lecrux et al., 2015); and Ppp2r5d deficiency causes tau pathology and behavioral defects in mice (Louis et al., 2011).

Annotation enrichment analysis of the interactors revealed their involvement in several key signaling pathways, such as "protein serine/threonine kinase activity", "GTPase regulator activity", and "protein phosphorylation" (Supplementary Fig. S5a-c). Another enriched category was "microtubule", consistent with the impaired morphology of β protein-expressing neurons (Fig. 1e-f). In addition to these general cellular pathways, we found neuron-specific categories, such as "synapse", "postsynaptic cell membrane" and "neuron projection" (Supplementary Fig. S5a-c). Of note, similar functional categories were revealed by interactome analyses of other aggregating proteins such as mutant Huntingtin (Hosp et al., 2015; Shirasaki et al., 2012). Previous proteomic investigations of aggregates demonstrated a marked enrichment of co-aggregating proteins in low-complexity regions (LCRs) (Hosp et al., 2017; Kim et al., 2016; Olzscha et al., 2011; Woerner et al., 2016). We therefore also quantified this property in β protein interactomes, and found a gradual increase in LCRs that paralleled the aggregation propensity (Supplementary Fig. S5d).

Analysis of the total proteome of transduced neurons (which includes the proteins sequestered in the aggregates) resulted in identification of almost 6,000 proteins in each of the conditions (Supplementary Fig. S6a, Supplementary Table S2). No significant changes were detected in the total levels of any of the β protein interactors, suggesting that their presence in the aggregates was not merely a result of their increased amounts in the cells, nor was their sequestration markedly compensated by increased expression (Supplementary Fig. S6b-d, Supplementary Tables S1 and S2). The unaltered total levels of the interactors, together with their enrichment in the aggregates,

suggest that the biologically active cellular pool of these proteins is likely to be reduced, potentially leading to functional impairments.

AP-3 μ 1 is sequestered by β protein aggregates and modifies β protein toxicity

The most highly enriched protein in the interactome of all three β proteins taken together was AP-3 μ 1, the medium subunit of the heterotetrameric AP-3 adaptor complex (Fig. 5b-e). The AP-3 complex is involved in intracellular trafficking of transmembrane proteins, including protein transport to lysosomes and lysosome-related organelles (Newell-Litwa et al., 2007). The medium subunit of the complex is responsible for cargo selection by recognizing the sorting signals on the cargo proteins (Ohno et al., 1998). AP-3 μ 1 made up 26% of the β 4-mCherry-interacting complexes, 17% for β 17-mCherry, and 10% for β 23-mCherry (Fig. 5f-h), while its amount in the total proteome was not significantly changed (Supplementary Fig. S6b-d). Immunofluorescence experiments in neurons co-transfected with Flag-AP-3 μ 1 and β 4-mCherry or β 23-mCherry confirmed a high degree of colocalization of AP-3 μ 1 with β proteins (Fig. 6a-b). Taken together, these data suggest that AP-3 μ 1 can be substantially sequestered by aggregates. As AP-3 μ 1 is not highly abundant in neurons (Supplementary Fig. S6e), its aberrant interaction with the aggregating proteins might result in a partial loss of function.

Previous proteomic studies also demonstrated interactions of AP-3 μ 1 and other subunits of the AP-3 complex with disease-related proteins including the Arctic mutant of $A\beta_{1-42}$ and mutant Huntingtin (mHTT) (Hosp et al., 2017; Olzscha et al., 2011; Shirasaki et al., 2012). Furthermore, mutations in the large β and δ subunits of the AP-3 complex lead to defects in biogenesis and function of lysosome-related organelles in mice and in humans with the rare genetic disorder Hermansky-Pudlak syndrome (Dell'Angelica, 2009). Thus, we hypothesized that AP-3 loss of function may play a role in the lysosomal defects observed in β protein-expressing neurons by impairing delivery of lysosomal proteins to these organelles. To test whether re-supplying AP-3 μ 1 would be sufficient to ameliorate the deleterious effects of β proteins, we quantified cell death in neuronal cultures co-transfected with β proteins and Flag-AP-3 μ 1 or EGFP as a control. Cleaved Caspase-3 staining demonstrated that co-expression of AP-3 μ 1 significantly reduced β protein-dependent toxicity in both β 4-mCherry and β 23-mCherry cells (Fig. 6c-d). Taken together, these data suggest that impaired formation and/or function of the AP-3 adaptor complex contributes to β protein toxicity in neurons.

Discussion

Here we show that artificial aggregating proteins without an evolved function engage in interactions with multiple cytoplasmic proteins and cause toxicity in primary neurons. The most conspicuous cellular defect caused by β proteins in neurons is an impairment of the autophagy-lysosomal pathway. The autophagy block likely occurs at a late step of the pathway, as autophagosome formation and autophagosome/lysosome fusion appear intact, but degradation of the autophagic cargo in the lysosomes is compromised.

The lysosomal abnormalities that we observed in β protein-expressing neurons are reminiscent of those reported in common neurodegenerative diseases such as Alzheimer's and Parkinson's (Dehay et al., 2012; Suzuki and Terry, 1967; Usenovic et al., 2012). One possible cause of lysosomal defects in protein misfolding disorders is that protein aggregates are targeted by the autophagy-lysosomal pathway (Filimonenko et al., 2010; Hoffmann et al., 2019; Jo et al., 2014; Menzies et al., 2015), but fail to be efficiently degraded upon delivery to lysosomes, accumulating in these organelles and impairing their function (Lamark and Johansen, 2012). Thus, dilated dysfunctional lysosomes were observed as a result of accumulation of α -synuclein aggregates within the lysosomal pathway (Hoffmann et al., 2019; Usenovic et al., 2012). However, in the case of β proteins, this scenario seems unlikely, since no aggregates were found within lysosomes by cryo-ET or light microscopy. Our results therefore suggest that lysosomal impairments are not just a consequence of the build-up of aggregates that overwhelm this degradation pathway.

Instead, we propose that impaired trafficking of lysosomal proteins due to an insufficient cellular pool of intact AP-3 complex may contribute to lysosomal defects caused by protein aggregates. As the μ -subunit is important for identifying the sorting signals on the cargo proteins (Ohno et al., 1998), its loss of function is likely to result in impaired cargo recognition. In addition, reduced levels of a single AP-3 subunit can compromise the assembly and stability of the complex (Peden et al., 2002). These defects in the AP-3 complex in turn lead to altered intracellular trafficking of lysosomal proteins, which

are then re-routed to the plasma membrane (Dell'Angelica et al., 1999), likely causing lysosomal dysfunction. Sequestration of functionally important lysosomal proteins by aggregates and impaired trafficking of lysosomal enzymes was also described in synucleinopathies and in spinal and bulbar muscular atrophy (Chu et al., 2009; Cortes et al., 2014; Decressac et al., 2013; Dehay et al., 2012; Mazzulli et al., 2016). Thus, a shortage of essential lysosomal components due to their sequestration and/or trafficking impairment might be a general feature of protein misfolding disorders. Importantly, restoration of AP-3 μ 1 expression was sufficient to significantly reduce β protein-dependent cell death. Whether restoring AP-3 function could be beneficial in other models of neurodegeneration is an interesting question for future research.

Previous studies of β proteins conducted in HEK cells revealed their multifactorial toxicity affecting many essential cellular processes (Olzscha et al., 2011). While our results are in agreement with these previous findings, our current multidisciplinary approach enabled us to specifically pinpoint lysosomal degradation as a pathway that is particularly vulnerable in primary neurons. Our results furthermore strengthen the connection between neurodegenerative diseases and lysosomal storage disorders, which has so far been demonstrated most convincingly for Parkinson's disease (Aflaki et al., 2017; Winder-Rhodes et al., 2012). The molecular links that were described between these two types of disorders include the feedback loop between oligomeric α -synuclein accumulation and deficiency of the lysosomal enzyme glucocerebrosidase, encoded by the GBA1 gene (Mazzulli et al., 2011). Mutations in GBA1 cause the lysosomal storage disorder Gaucher disease, and are also the most common genetic risk factor for Parkinson's disease and other synucleinopathies (Aflaki et al., 2017). Moreover, Parkinson's disease patients often carry pathological variants of other lysosomal storage disorder genes (Robak et al., 2017). Our results suggest that the presence of misfolded proteins can also cause lysosomal storage through an indirect effect on the availability and trafficking of functionally important lysosomal proteins. In summary, our findings support the notion that impairment of the autophagy-lysosomal degradation pathway is a crucial event in neurodegenerative proteinopathies.

Materials and Methods

Lentivirus production

Hek293T cells for lentiviral packaging were purchased (Lenti-X 293T cell line, Takara) and expanded to 70-85% confluency in DMEM Glutamax (+ 4.5g/L D-Glucose, - Pyruvate) supplemented with 10% FBS (Sigma), 1% G418 (Gibco), 1% NEAA (Thermo Fisher), 1% HEPES (Biomol). Only low passage cells were used. For lentiviral production, three T75cm² flasks (Falcon) containing 5.7 million cells each were seeded and henceforth cultured in medium without G418. On the following day, cells were transfected with the expression plasmid pFhSynW2, and the packaging plasmids psPAX2 and pVsVg (all three kindly provided by Prof. Dieter Edbauer) using TransIT-Lenti transfection reagent (Mirus). The transfection mix was incubated for 20 min at room temperature (RT) and in the meanwhile, cell medium was exchanged. 1 ml transfection mix was added to each flask and left overnight. The medium was exchanged on the next day. After 48-52 h, culture medium containing the viral particles was collected and centrifuged for 10 min at 1200 x g. Then, the supernatant was filtered through 0.45 µm pore size filters using 50 ml syringes, transferred to Ultra-clear centrifuge tubes (Beckman), and centrifuged at 100,000 x g for 2 h with in the Avanti JXN-30 centrifuge, rotor JS-24.38 (Beckman). Supernatant was discarded and the lentivirus pellet resuspended in TBS-5 buffer (50 mM Tris-HCl, pH 7.8, 130 mM NaCl, 10 mM KCl, 5 mM MgCl₂). After aliquoting, virus was stored at -80°C. For interactome analyses, lentivirus was produced using the pLV-Syn vector (derived from pLenti7.3-V5-Dest) and the packaging vectors pCMVdelta8.91 and pMD2_G (kindly provided by Dr. Alexandra Lepier).

Preparation of EM grids

R 2/1 Holey Carbon Au 200 mesh EM grids (Quantifoil) were coated with approximately 20 nm of carbon in a MED 020 carbon coater (BAL-TEC) and made hydrophilic for 45 s in a PDC-3XG plasma cleaner (Harrick). For HeLa cell culture, the grids were UV-sterilized in a Herasafe HR18 cell culture hood (Heraeus) for 30 min. For neuronal cultures, the grids were sterilized in ethanol for 10 min, washed several times in double-distilled water and transferred to culture dishes containing water. Grids and dishes for neuronal cultures were coated with poly-D-lysine (Sigma-Aldrich; 1 mg/ml in borate buffer) for 24 h and washed three times with water. Subsequently, the grids were coated with laminin (Thermo Fisher; 5.0 µg/ml in PBS) for 24 h, washed with PBS three times and placed in

Neurobasal medium supplemented with B27 containing 0.5 mM Glutamine (all reagents from Thermo Fisher). During washes and medium exchange steps, grids were transferred into another dish containing the appropriate liquid to prevent them from drying.

Primary neuron culture

Primary neurons were prepared from E14.5-15.5 CD-1 or C57BL/6 wildtype embryos. Pregnant mice were sacrificed by cervical dislocation, the uterus was removed from the abdominal cavity and placed into a 10 cm sterile Petri dish on ice containing dissection medium, consisting of Hanks' balanced salt solution (HBSS) supplemented with 0.01 M HEPES, 0.01 M MgSO₄, and 1% Penicillin / Streptomycin. Each embryo was isolated, heads were quickly cut, brains were removed from the skull and immersed in ice-cold dissection medium. Subsequently, cortical hemispheres were dissected and meninges were removed under a stereo-microscope. For each sample, cortical or hippocampal tissue from typically six to seven embryos was transferred to a 15 ml sterile tube and digested with 0.25% trypsin containing 1 mM 2,2',2'',2'''-(ethane-1,2-diyldinitrilo) tetraacetic acid (EDTA) and 15 µl 0.1% DNase I for 20 minutes at 37°C. The enzymatic digestion was stopped by removing the supernatant and washing the tissue twice with Neurobasal medium (Invitrogen) containing 5% FBS. The tissue was resuspended in 2 ml medium and triturated to achieve a single-cell suspension. Cells were spun at 130-180 x g, the supernatant was removed, and the cell pellet was resuspended in Neurobasal medium with 2% B27 (Invitrogen), 1% L-Glutamin (Invitrogen) and 1% Penicillin/Streptomycin (Invitrogen). For cryo-ET, Neurons were plated on the coated grids within 24-well plates (60,000 per well). For MS analysis, cells were cultured on 6 well-plates (Thermo Fisher Scientific) (500,000 neurons per well) coated with 1 mg/ml Poly-D-Lysine (Sigma) and 1 µg/ml Laminin (Thermo Fisher Scientific). For immunostaining, neurons were cultured on 13 mm coverslips, coated as above, in 24 well-plates (Thermo Fisher Scientific). For MTT assay, neurons were cultured in coated 96 well-plates. Transfection was performed using Calcium Phosphate according to the protocol from (Jiang and Chen, 2006) or using Lipofectamine2000 (Thermo Fisher Scientific) according to the manufacturer's protocol. For lentiviral transduction, viruses were thawed and immediately added to freshly prepared neuronal culture medium. A fifth of the medium from cultured neurons was removed and the equivalent volume of virus-containing medium was added. Typically, 1

$\mu\text{l}/\text{cm}^2$ of virus was added, but this amount was sometimes adjusted to match protein expression levels among different constructs.

HeLa cell culture

HeLa CCL-2 (ATCC) cells were grown in DMEM medium (Life Technologies) with 10% FBS (Life Technologies), 0.5 mM L-Glutamine (Life Technologies), 1% MEM NEAA 100x (Life Technologies), 1% Penicillin/Streptomycin (10,000 U/mL; Life Technologies) at 37°C and 5% CO₂. Before experiments, the medium was exchanged for medium without Penicillin/Streptomycin. For cryo-ET, approximately 25,000 cells were seeded in 35 mm culture dishes (BD Falcon) containing four pre-treated EM grids 24 h prior to transfection. For western blot experiments, cells were plated in 6 cm dishes 24 h prior to transfection. HeLa cells were transfected using FuGENE 6 transfection reagent (Promega) according to the manufacturer's instructions, and harvested 24 h after transfection.

Immunostaining

Cells were fixed with 4% Paraformaldehyde in PBS for 20 min; remaining free groups of PFA were blocked with 50 mM Ammonium chloride in PBS for 10 min at RT. Cells were rinsed once with PBS and permeabilized with 0.25% Triton X-100 in PBS for 5 min. After permeabilization, cells were washed with PBS and blocked with 2% BSA (w/v) (Roth) and 4% donkey serum (v/v) (Jackson ImmunoResearch Laboratories) in PBS for 30 min at RT. Coverslips were transferred to a light-protected humid chamber and incubated in primary antibody diluted in blocking solution for 1 h. The following primary antibodies were used: anti-mCherry (AB0040-200, Origene, 1:500), anti-myc 9E10 (13-2500, Thermo Fisher, 1:100), anti-cleaved Caspase-3 (9661S, CST, 1:500) and anti-Flag (TA-50011-100; Origene, 1:500). Cells were washed with PBS and incubated with secondary antibodies (Jackson ImmunoResearch Laboratories) diluted 1:250 in blocking solution, with 1:2000 1 mg/ml DAPI added to stain the nuclei. Coverslips were mounted on Menzer glass slides using Dako or Prolong fluorescence mounting medium. Confocal images were obtained at a spinning disc microscope (Zeiss) or SP8 confocal microscope (Leica).

Colocalization analysis was performed on single plane images of double-transfected neurons. A ROI was manually drawn around the soma of each cell in the mCherry channel and the ImageJ plug-in Coloc 2 was used to calculate the Pearson's correlation coefficient.

Neuronal viability measurements and Sholl analysis

For transduced neurons, viability was determined with the MTT assay using Thiazolyl Blue Tetrazolium Bromide (MTT) reagent purchased from Sigma-Aldrich. Neurons were cultured in 96-well plates. First, cell medium was exchanged for 100 μ l of fresh medium. Then, 20 μ l of 5 mg/ml MTT in PBS was added and incubated for 2-4 h at 37°C, 5% CO₂. Subsequently, 100 μ l solubilizer solution (10% SDS, 45% Dimethylformamide in water, pH 4.5) was added, and on the following day absorbance was measured at 570 nm. Each condition was measured in triplicates and absorbance values averaged for each experiment.

For transfected neurons, toxicity was quantified by an investigator blinded to the conditions based on immunostaining for cleaved caspase-3. In bafilomycin-treated cultures, viability was primarily assessed by nuclear condensation, and additionally verified by cleaved caspase-3 staining.

For Sholl analysis, mCherry channel was used to visualize neuronal morphology. Coverslips were immunostained against mCherry and imaged with a 40x objective. Maximum intensity projections were analyzed. First, cell morphologies were semiautomatically traced with the Simple Neurite Tracer plug-in of ImageJ in a blinded way. Then, complexity of the traced neurons was quantified with the Sholl analysis plug-in of ImageJ using a custom-made macro for batch processing.

Sample vitrification

Cells were vitrified using a home-made manual gravity-driven plunge-freezer. Before plunge-freezing, cells were treated with 10% glycerol (Sigma-Aldrich) in medium as a cryoprotectant for 1 – 5 min. In addition, in some cases cells were stained with 3% Annexin V, Alexa Fluor 488 conjugate (Life Technologies) 15 minutes prior to vitrification to identify dead cells. During plunge-freezing, EM grids were blotted for 8 s with filter paper No. 1 (Whatman) from the back side and immediately frozen in liquid ethane/propane (37% / 63%; Linde) kept at liquid nitrogen temperature. Grids were transferred to liquid nitrogen and excess ethane/propane was blotted with pre-cooled filter paper. Grids were stored in liquid nitrogen until further use.

Cryo-light microscopy

Frozen grids were fixed into FIB C-clip rings to increase mechanical stability. Samples were transferred to a CorrSight shuttle (FEI) and mounted on the CorrSight cryo-stage (FEI) maintained at liquid nitrogen temperature for cryo-light microscopy. Samples were imaged using widefield or spinning-disk confocal, epifluorescence microscopy using FEI MAPS 2.1 software. Images were acquired with a 1344 x 1024 pixel camera (pixel size 6.4 μm , Hamamatsu Digital Camera C10600 ORCA-R2). Grids were imaged in widefield mode at low magnification with a 5x air objective (Plan-ApoChromat, NA 0.16; Carl Zeiss) and in spinning-disk confocal mode at high magnification with a 40x air objective (EC Plan-Neofluar, NA 0.9; Carl Zeiss) for identification of cells and/or aggregates. Image acquisition and further SEM correlation was performed by three-point correlation using FEI MAPS 2.1 software.

Cryo FIB SEM

Grids imaged by light microscopy were mounted on a transfer shuttle designed for a cryo-loading system (Rigort et al., 2010) and loaded into a Quanta 3D FEG dual-beam FIB/SEM (FEI). Grids were sputtered with platinum (10 mA, 30 s) in a PP3000T loading system (Quorum) to reduce charging effects during electron imaging. Grids were loaded into the FIB chamber and coated with organometallic platinum as a protective layer for ion beam milling. Grids were imaged with the scanning electron beam operated at 5 kV / 12 pA and regions of interest (ROI) were identified via cryo-LM/SEM 3-point correlation using MAPS 2.1 software. ROIs were thinned down at tilt angles of 18° - 20° with the focused ion beam operated at 30 kV. The beam currents were set to 1 nA at approximately 1 μm distance from the ROI, 500 pA at 750 nm, 300 pA at 400 nm, 100 pA at 250 nm, 50 pA at 100 nm and 30 pA at 75 nm for polishing. Grids were sputtered once more with platinum (10 mA, 5 s) after milling to increase conductivity of the lamellae for VPP imaging.

Cryo ET

Cryo-TEM was performed on a Titan Krios cryo-TEM (FEI) operated at 300 kV, equipped with a FEG, post-column energy filter (Gatan) and Volta phase plate (Danev et al., 2014). Tomograms were acquired on a K2 Summit direct electron detector (Gatan) in dose fractionation mode (0.08 frames per second) using SerialEM (Mastronarde, 2005). Lamella overview images were acquired at 3600x magnification (pixel size: 38.93 \AA) and stitched using the automatic photo merge in Adobe Photoshop.

For cryo-LM – cryo-TEM correlation, stitched lamella TEM overview images were imported into MAPS and aligned with cryo-LM data. Tilt series were recorded at -0.5 μm defocus for VPP imaging at 33000x magnification (pixel size: 4.21 \AA), with an angular increment of 2° and typically ranged from -50° to 60° . The total dose was restricted to approximately 120 electrons / \AA^2 per tomogram.

Tomogram reconstruction and data processing

K2 frames were aligned and combined using an in-house software based on previous work (Li et al., 2013). Tilt-series were aligned using patch tracking from the IMOD software package (Kremer et al., 1996) and reconstructed by weighted back projection. The platinum layer for VPP imaging and large pieces of surface ice contamination were computationally removed to increase signal-to-noise ratio (Fernandez et al., 2016). The resulting tilt-series were realigned and reconstructed again. Tomograms were binned four times to a final pixel size of 16.84 \AA to increase contrast.

Tomogram segmentation was performed using Amira (FEI). Membranes and microtubules were automatically segmented using TomoSegMemTV (Martinez-Sanchez et al., 2014) and corrected using Amira. β -protein fibrils were traced on denoised tomograms (non-local means filter) by removing membranes and macromolecules followed by density thresholding and subsequent skeletonization. For the identification of ribosome positions, template matching was applied using the pyTOM toolbox in MATLAB (Mathworks) as previously reported (Hrabe et al., 2012). A human 80S ribosome structure (PDB: 4UG0) (Khatter et al., 2015) was filtered to 40 \AA and used as a template. Coordinates of ribosomes identified via template matching were imported into Amira and masked with the filtered molecular structure.

Live cell light microscopy

Samples were imaged using brightfield and epifluorescence widefield microscopy in a CorrSight microscope (FEI) using FEI MAPS 2.1 software. Low magnification overview images were acquired with a 5x air objective (Plan-ApoChromat, NA 0.16; Carl Zeiss). For high magnification image stacks, a 63x oil immersion objective (Plan Achromat, NA 1.4; Carl Zeiss) was used. Cells were kept on a 37°C heated stage in a homemade climate chamber infused with humidified air and 5% CO_2 gas. Cells were located at low magnification and z-stacks were acquired in 500 nm steps over the whole cell height at high magnification.

For the analysis of lysosome size and number, neuronal cultures expressing β 23-mCherry, β 4-mCherry or mCherry were incubated with 75 nM LysoTracker Green DND-26 (Thermo Fisher Scientific) for 30 min according to manufacturer's instructions. The mCherry signal was used to assess the cell perimeter and only lysosomes within that perimeter were measured. The mCherry signal of each cell was isolated by automatic thresholding using a homemade script written for Fiji software (Schindelin et al., 2012). The size of each lysosome was manually measured in its in-focus plane using Fiji software. The Pearson correlation coefficient was measured using JACoP plugin in Fiji software (Bolte and Cordelieres, 2006).

Western Blotting

Primary neurons were lysed in 50 mM Tris-HCl, pH 7.4, 150 mM NaCl, 2 mM EDTA, 1% Triton X-100. Lysates were centrifuged for 10 min at 4,000 x g and 4°C and supernatants collected, mixed with 6x loading buffer, and boiled for 5 min at 95°C. Samples were separated in 12% SDS-PAGE gels and blotted onto PVDF membranes using a Trans-Blot Turbo transfer system (Bio-Rad). Blocking was performed with 3% BSA, 5% dried milk (Roth) in TBS-T for 1 h at RT. Primary antibodies were diluted 1:1000 in 3% BSA in TBS-T, 0.01% Sodium azide and incubated for 2 days at 4°C. Secondary HRP-conjugated antibodies (Jackson ImmunoResearch) were diluted 1:5000 in 5% dried milk in TBS-T and applied for 2 h at RT. Detection was performed using ECL detection reagent (GE Healthcare) in a Peqlab Fusion Fx7 chemiluminescence imaging system. Primary antibodies used were anti-myc 9E10 (13-2500, Thermo Fisher) and anti-Tubulin (T9026, Sigma). Band density quantification was performed with ImageJ.

Whole-cell extracts of cultured HeLa cells were prepared in 1.5% n-Dodecyl β -D-maltoside (Sigma-Aldrich) in PBS as described (Raimundo et al., 2009). Gels were loaded with 50 μ g of total protein per well, proteins were separated in 15% SDS-PAGE gels and transferred to PVDF membranes. The following primary antibodies were used for immunoblotting: Atg5 (D5F5U) Rabbit mAb (Cell Signaling), Beclin-1 antibody (Cell Signaling), Anti-HPRT antibody (Abcam), Anti-LAMP1 antibody (Abcam), LC3B (D11) XP® Rabbit mAb (Cell Signaling). Band density quantification was performed with ImageJ and normalized against loading controls.

Quantitative RT-PCR

RNA isolation and purification was performed using a Crystal RNA mini Kit (Biolab) according to the manufacturer's instructions. RNA quantification and quality control were done with a Nanodrop spectrophotometer (PiqLab). cDNA was synthesized using a High-Capacity cDNA Reverse Transcription Kit (Applied Biosystems) according to the manufacturer's instructions. cDNA was diluted 1:50, each 8 μ l reaction contained 4 μ l diluted cDNA, 0.2 μ l dilutions of each primer (25 μ M stock), and 3.6 μ l Luna Universal Probe qPCR Master Mix (New England BioLabs). The primers were described previously (Fernandez-Mosquera et al., 2017).

Immunoprecipitation

Interactome analysis was conducted in four independent biological replicates. Lysis of cortical neurons (500.000 cells/condition) was performed in ice-cold lysis buffer (0,25% NP40, 5% glycerol, 50 mM Tris HCl, 150 mM NaCl) containing protease inhibitor (Roche), DNase (5 μ l/ml) and RNase (0,5 μ l/ml). Thermo Scientific™ Pierce™ Protein G Agarose (10 μ l/100 μ g IgG) was used for purification and immunoprecipitation of IgG antibodies. Serum samples containing IgG were incubated with Protein G agarose in a buffer that facilitates binding (20 mM sodium phosphate) for 1 h. Then, neuronal lysates were loaded onto IgG-protein G Agarose and incubated for 4 h. Non-IgG and non-antigen components were discarded from the sample by washing with 0,1% NP40, 5% Glycerol, 50 mM Tris HCl, 150 mM NaCl. Enriched proteins were next isolated and processed in a step-wise manner. First, proteins were denatured, digested and cysteines reduced for 1 hour at 20°C by adding 8 M Urea, 40 mM Hepes pH 8.0, 1 μ g LysC and 10 mM DTT. Next, urea concentration was lowered to 2 M by adding 50 mM ammonium bicarbonate in MilliQ water. Trypsin (1 μ g) was added to the protein-peptide mix and samples were subjected to 55 mM chloroacetamide for 1 h to alkylate cysteine residues. Alkylation was quenched by adding 2 M urea / 50 mM thiourea and overnight digestion was carried out after addition of 1 μ g fresh trypsin.

Complete neuronal proteome precipitation

Complete neuronal proteomes were extracted as described previously (Hornburg et al., 2014). In brief, cells were lysed in lysis buffer (4% SDS, 10 mM Hepes, pH 8.0) and reduced with 10 mM DTT for 30 min. The proteins were then subjected to 45 min of alkylation with 55 mM iodoacetamide. Acetone precipitation was performed to remove the SDS: Acetone (-20 °C) was added to 100 μ g of

proteins to a final concentration of 80% v/v, and proteins were precipitated overnight at -20 °C. The supernatant was removed after 15 min of centrifugation (4 °C, 16,000 x g) followed by washing with 80% acetone (-20 °C). Residual acetone was evaporated at 20°C. The protein pellet was dissolved in 50 µl of 6 M urea/2 M thiourea, 10 mM Hepes, pH 8.0. LysC (1 µg) digestion was carried out for 2 h at 20°C. The samples were incubated with 1 µg trypsin for overnight digestion, and peptides were desalted on C18 solid phase extraction.

Solid phase extraction

Stage Tips were prepared with 3xC18 material for rapid desalting and step elution of the peptide mixtures. Stage Tips were rinsed with MeOH and Buffer A (0.5% acetic acid). Samples were added to the staging tips and washed with buffer A. Buffer B (80% Acetonitrile, 0.5% acetic acid) was used to elute the samples. Speedvac was used to remove the solvent from the samples. The samples were then resuspended in 10 µl buffer A* (0.5% AcOH, 0.1% TFA, 2% ACN).

LC-MS/MS

Peptides were separated on EASY-nLC 1000 HPLC system (Thermo Fisher Scientific, Odense, Denmark). Columns (75-µm inner diameter, 40-cm length) were in-house packed with 1.9-µm C18 particles (Dr. Maisch GmbH, Ammerbuch-Entringen, Germany). Peptides were loaded in buffer A (0.5% formic acid) and separated with a gradient from 7% to 60% buffer B (80% acetonitrile, 0.5% formic acid) within 3.5 h at 200 nl/min. The column temperature was set to 60 °C. A quadrupole Orbitrap mass spectrometer (Q Exactive, Thermo Fisher Scientific) was directly coupled to the liquid chromatograph via a nano-electrospray source. The Q Exactive was operated in a data-dependent mode. The survey scan range was set to 300 to 1,650 m/z, with a resolution of 70,000 at m/z 200. Up to 15 most abundant isotope patterns with a charge of ≥ 2 were subjected to Higher-energy collisional dissociation (Olsen et al., 2007) with a normalized collision energy of 25, an isolation window of 2 Th, and a resolution of 17,500 at m/z 200. To limit repeated sequencing, dynamic exclusion of sequenced peptides was set to 30 s. Thresholds for ion injection time and ion target value were set to 20 ms and 3×10^6 for the survey scans and to 60 ms and 10^6 for the MS/MS scans. Data were acquired using Xcalibur software (Thermo Scientific).

MS data analysis

To process MS raw files, we employed MaxQuant software (v. 1.5.7.10) (Cox & Mann, 2008). Andromeda (Cox et al., 2011), which is integrated into MaxQuant, was used to search MS/MS spectra against the UniProtKB FASTA database. For the standard immunoprecipitation and pre-loaded serum, enzyme specificity was set to trypsin and LysC. For all the experiments, N-terminal cleavage to proline and up to two miscleavages were allowed. Peptides with a minimum length of seven amino acids were considered for identification. Oxidation, acetylation and deamidation were set as variable modifications (maximum number of modifications per peptide was 5). A false discovery rate (FDR) cut-off of 1% was applied at the peptide and protein levels. Initial precursor mass deviation of up to 4.5 ppm and fragment mass deviation up to 20 ppm were allowed. Precursor ion mass accuracy was improved by time-dependent recalibration algorithms in MaxQuant. The cut-off score (delta score) for accepting individual MS/MS spectra was 17.

The proteome fasta file from *Mus musculus* (Taxon identifier: 10090) was used as a library for matches. Nonlinear retention time alignment (Cox and Mann, 2008; Cox et al., 2011) of all measured samples was performed in MaxQuant. "Match between runs," which allows the transfer of peptide identifications in the absence of sequencing, was enabled with a maximum retention time window of 0.7 min. Furthermore, we filtered our data by requiring a minimum peptide ratio count of 1 in MaxLFQ. Protein identification required at least one razor peptide (Cox and Mann, 2008). Proteins that could not be discriminated on the basis of unique peptides were grouped into protein groups. Co-immunoprecipitated proteins were considered interactors if they were significantly enriched compared to the control samples applying a 5% permutation-based FDR cut-off (see below).

For statistical and bioinformatic analysis, as well as for visualization, we used the open Perseus environment, which is part of MaxQuant. The numerical data was transformed to $\log_2(x)$. Proteins were filtered for common contaminants; proteins identified only by site modification and reverse proteins were excluded. Missing values in pairwise comparisons were imputed with a normal distribution (width = 0.3 x standard deviation; down shift = 1.8 x standard deviation) was performed in Perseus. Proteins were only considered if they were detected with at least three valid values among quadruplicates in at least one condition. For pairwise comparison of proteomes and determination of significant differences in protein abundances, t-test statistics were applied with a permutation-based FDR of 5% and S_0 of 1. The resulting significant outliers for each of the sample pairs were analyzed

for gene ontology (GOCC) (Harris et al., 2004), biological ontology (GOBP), Molecular function (GOMF), protein complexes (CORUM) (Ruepp et al., 2010), and protein families and domains (Pfam) (Finn et al., 2014) annotation enrichments. The data was displayed in a scatter plot for visual representation. For protein abundance ranking, summed peptide intensities from MaxQuant (median of at least 3 valid values within quadruplicates) were divided by the molecular weight to adjust for protein size bias and estimate the abundance rank of each protein within the proteome. Log₁₀ corrected intensities were plotted against the rank.

To calculate the content of disordered regions, we employed R (rjson and seqinr libraries). First, amino acids that are predicted with low complexity long region (IUPred-L) were mapped to sequences of proteins that are significant outliers in either of the β protein interactomes as well as for the entire population of proteins identified in the interactomes. Next, the ratio of all amino acids and those predicted with low complexity was calculated. To determine the significance of differences between the individual populations, a two-sample Wilcoxon test was performed on the ratio distributions.

Aggregate composition estimation

To estimate the relative mass composition of the protein aggregates, the median of log₂ MaxLFQ intensity (requiring at least 2 valid values) was calculated across quadruplicates for the β protein samples and the mCherry controls, respectively. Missing values in the mCherry samples were imputed with a normal distribution on the log₂ scale (width = 0.3 x standard deviation; down shift = 1.8 x standard deviation). Next, the non-log (median) intensity of each protein in the β protein samples was subtracted by the respective non-log intensity derived from the mCherry samples. This transformation corrects for the overall background signal in the immunoprecipitation. The resulting intensities roughly correspond to the relative abundance in the aggregate (= composition) and are plotted as fractions in pie charts. Note that we did not apply an FDR or p-value cut-off for this analysis. By subtracting protein intensity of the mCherry controls from those in the β protein samples, small differences (which associate with larger p-values and FDRs) have a diminishing contribution to the overall aggregate composition estimate. In the pie charts, proteins with at least 3% intensity contribution are listed.

Statistical analysis

Statistical analysis of the MS data is described in the previous section. Statistical analysis of other data was performed using Origin Pro 2015G or GraphPad Prism 6. Data are presented as means \pm standard deviation unless indicated otherwise.

Acknowledgements

We thank F. Ulrich Hartl and Mark S. Hipp for sharing reagents and helpful discussions; Günter Pfeifer, Jürgen Plitzko and Miroslava Schaffer for electron microscopy support; Qiang Guo for ribosome template matching; Alexandra Lepier, Dieter Edbauer and Carina Lehmer for lentiviral plasmids and generous help with lentivirus generation; Martin Dodel and Patrick Auer for excellent technical assistance; Daniel del Toro Ruiz for kind help with image analysis; and Shivani Tiwary for discussions. This work was funded by the European Research Council (ERC) Synergy Grant under FP7 GA number ERC-2012-SyG_318987-Toxic Protein Aggregation in Neurodegeneration (ToPAG) (to M.M., W.B. and R.K.); ERC Starting Grant MitoPexLysoNETWORK 337327 (to N.R.); Deutsche Forschungsgemeinschaft (DFG, German Research Foundation) through Germany's Excellence Strategy - EXC 2067/1- 390729940 (to R.F.-B.); and by the Max Planck Society for the Advancement of Science.

Author contributions

T.S. performed cryo-ET and LysoTracker experiments. I.R.-T. characterized β proteins in transfected and transduced neurons, performed AP-3 μ 1/ β protein colocalization analysis, and prepared neurons for proteomic analysis. D.H. performed proteomic analysis. A.M. quantified cell death in neurons coexpressing β proteins and AP-3 μ 1 and upon bafilomycin treatment, and prepared neurons for cryo-ET. L.F.-M. and N.R. performed Western blots and RT-PCR for autophagy-lysosomal markers. T.S., I.R.-T., D.H. and I.D. prepared the figures. M.M., W.B., R.K., F.M., R.F.-B. and I.D. designed research. F.M., R.F.-B. and I.D. supervised research. R.F.-B. and I.D. wrote the paper with input from all authors.

Conflict of interest

The authors declare no competing interests.

References

- Abeliovich, A., and A.D. Gitler. 2016. Defects in trafficking bridge Parkinson's disease pathology and genetics. *Nature*. 539:207-216.
- Aflaki, E., W. Westbroek, and E. Sidransky. 2017. The Complicated Relationship between Gaucher Disease and Parkinsonism: Insights from a Rare Disease. *Neuron*. 93:737-746.
- Armstrong, L., R. Biancheri, C. Shyr, A. Rossi, G. Sinclair, C.J. Ross, M. Tarailo-Graovac, W.W. Wasserman, and C.D. van Karnebeek. 2014. AIMP1 deficiency presents as a cortical neurodegenerative disease with infantile onset. *Neurogenetics*. 15:157-159.
- Bauerlein, F.J.B., I. Saha, A. Mishra, M. Kalemanov, A. Martinez-Sanchez, R. Klein, I. Dudanova, M.S. Hipp, F.U. Hartl, W. Baumeister, and R. Fernandez-Busnadiego. 2017. In Situ Architecture and Cellular Interactions of PolyQ Inclusions. *Cell*. 171:179-187 e110.
- Bolte, S., and F.P. Cordelières. 2006. A guided tour into subcellular colocalization analysis in light microscopy. *J Microsc.* 224:213-232.
- Brothers, H.M., M.L. Gosztyla, and S.R. Robinson. 2018. The Physiological Roles of Amyloid-beta Peptide Hint at New Ways to Treat Alzheimer's Disease. *Front Aging Neurosci*. 10:118.
- Chiti, F., and C.M. Dobson. 2017. Protein Misfolding, Amyloid Formation, and Human Disease: A Summary of Progress Over the Last Decade. *Annu Rev Biochem*. 86:27-68.
- Chu, Y., H. Dodiya, P. Aebischer, C.W. Olanow, and J.H. Kordower. 2009. Alterations in lysosomal and proteasomal markers in Parkinson's disease: relationship to alpha-synuclein inclusions. *Neurobiol Dis*. 35:385-398.
- Cortes, C.J., H.C. Miranda, H. Frankowski, Y. Batlevi, J.E. Young, A. Le, N. Ivanov, B.L. Sopher, C. Carromeu, A.R. Muotri, G.A. Garden, and A.R. La Spada. 2014. Polyglutamine-expanded androgen receptor interferes with TFEB to elicit autophagy defects in SBMA. *Nature neuroscience*. 17:1180-1189.
- Cox, J., and M. Mann. 2008. MaxQuant enables high peptide identification rates, individualized p.p.b.-range mass accuracies and proteome-wide protein quantification. *Nat Biotechnol*. 26:1367-1372.
- Cox, J., N. Neuhauser, A. Michalski, R.A. Scheltema, J.V. Olsen, and M. Mann. 2011. Andromeda: a peptide search engine integrated into the MaxQuant environment. *J Proteome Res*. 10:1794-1805.
- Cuervo, A.M., L. Stefanis, R. Fredenburg, P.T. Lansbury, and D. Sulzer. 2004. Impaired degradation of mutant alpha-synuclein by chaperone-mediated autophagy. *Science*. 305:1292-1295.
- Danev, R., B. Buijse, M. Khoshouei, J.M. Plitzko, and W. Baumeister. 2014. Volta potential phase plate for in-focus phase contrast transmission electron microscopy. *Proc Natl Acad Sci U S A*. 111:15635-15640.
- Decressac, M., B. Mattsson, P. Weikop, M. Lundblad, J. Jakobsson, and A. Bjorklund. 2013. TFEB-mediated autophagy rescues midbrain dopamine neurons from alpha-synuclein toxicity. *Proc Natl Acad Sci U S A*. 110:E1817-1826.
- Dehay, B., A. Ramirez, M. Martinez-Vicente, C. Perier, M.H. Canron, E. Doudnikoff, A. Vital, M. Vila, C. Klein, and E. Bezard. 2012. Loss of P-type ATPase ATP13A2/PARK9 function induces general lysosomal deficiency and leads to Parkinson disease neurodegeneration. *Proc Natl Acad Sci U S A*. 109:9611-9616.
- Dell'Angelica, E.C. 2009. AP-3-dependent trafficking and disease: the first decade. *Curr Opin Cell Biol*. 21:552-559.
- Dell'Angelica, E.C., V. Shotelersuk, R.C. Aguilar, W.A. Gahl, and J.S. Bonifacino. 1999. Altered trafficking of lysosomal proteins in Hermansky-Pudlak syndrome due to mutations in the beta 3A subunit of the AP-3 adaptor. *Mol Cell*. 3:11-21.
- Fernandez, J.J., U. Laugks, M. Schaffer, F.J. Bauerlein, M. Khoshouei, W. Baumeister, and V. Lucic. 2016. Removing Contamination-Induced Reconstruction Artifacts from Cryo-electron Tomograms. *Biophys J*. 110:850-859.
- Fernandez-Mosquera, L., C.V. Diogo, K.F. Yambire, G.L. Santos, M. Luna Sanchez, P. Benit, P. Rustin, L.C. Lopez, I. Milosevic, and N. Raimundo. 2017. Acute and chronic mitochondrial respiratory chain deficiency differentially regulate lysosomal biogenesis. *Sci Rep*. 7:45076.

- Filimonenko, M., P. Isakson, K.D. Finley, M. Anderson, H. Jeong, T.J. Melia, B.J. Bartlett, K.M. Myers, H.C. Birkeland, T. Lamark, D. Krainc, A. Brech, H. Stenmark, A. Simonsen, and A. Yamamoto. 2010. The selective macroautophagic degradation of aggregated proteins requires the PI3P-binding protein Alfy. *Mol Cell*. 38:265-279.
- Finkbeiner, S. 2019. The Autophagy Lysosomal Pathway and Neurodegeneration. *Cold Spring Harbor perspectives in biology*.
- Finn, R.D., A. Bateman, J. Clements, P. Coggill, R.Y. Eberhardt, S.R. Eddy, A. Heger, K. Hetherington, L. Holm, J. Mistry, E.L. Sonnhammer, J. Tate, and M. Punta. 2014. Pfam: the protein families database. *Nucleic Acids Res*. 42:D222-230.
- Fraldi, A., A.D. Klein, D.L. Medina, and C. Settembre. 2016. Brain Disorders Due to Lysosomal Dysfunction. *Annu Rev Neurosci*. 39:277-295.
- Frottin, F., F. Schueder, S. Tiwary, R. Gupta, R. Korner, T. Schlichthaerle, J. Cox, R. Jungmann, F.U. Hartl, and M.S. Hipp. 2019. The nucleolus functions as a phase-separated protein quality control compartment. *Science*. 365:342-347.
- Gruber, A., D. Hornburg, M. Antonin, N. Kraemer, J. Collado, M. Schaffer, G. Zubaite, C. Luchtenborg, T. Sachsenheimer, B. Brugger, M. Mann, W. Baumeister, F.U. Hartl, M.S. Hipp, and R. Fernandez-Busnadiego. 2018. Molecular and structural architecture of polyQ aggregates in yeast. *Proc Natl Acad Sci U S A*. 115:E3446-E3453.
- Guo, Q., C. Lehmer, A. Martinez-Sanchez, T. Rudack, F. Beck, H. Hartmann, M. Perez-Berlanga, F. Frottin, M.S. Hipp, F.U. Hartl, D. Edbauer, W. Baumeister, and R. Fernandez-Busnadiego. 2018. In Situ Structure of Neuronal C9orf72 Poly-GA Aggregates Reveals Proteasome Recruitment. *Cell*. 172:696-705 e612.
- Harris, M.A., J. Clark, A. Ireland, J. Lomax, M. Ashburner, R. Foulger, K. Eilbeck, S. Lewis, B. Marshall, C. Mungall, J. Richter, G.M. Rubin, J.A. Blake, C. Bult, M. Dolan, H. Drabkin, J.T. Eppig, D.P. Hill, L. Ni, M. Ringwald, R. Balakrishnan, J.M. Cherry, K.R. Christie, M.C. Costanzo, S.S. Dwight, S. Engel, D.G. Fisk, J.E. Hirschman, E.L. Hong, R.S. Nash, A. Sethuraman, C.L. Theesfeld, D. Botstein, K. Dolinski, B. Feierbach, T. Berardini, S. Mundodi, S.Y. Rhee, R. Apweiler, D. Barrell, E. Camon, E. Dimmer, V. Lee, R. Chisholm, P. Gaudet, W. Kibbe, R. Kishore, E.M. Schwarz, P. Sternberg, M. Gwinn, L. Hannick, J. Wortman, M. Berriman, V. Wood, N. de la Cruz, P. Tonellato, P. Jaiswal, T. Seigfried, R. White, and C. Gene Ontology. 2004. The Gene Ontology (GO) database and informatics resource. *Nucleic Acids Res*. 32:D258-261.
- Hartl, F.U. 2017. Protein Misfolding Diseases. *Annu Rev Biochem*. 86:21-26.
- Hoffmann, A.C., G. Minakaki, S. Menges, R. Salvi, S. Savitskiy, A. Kazman, H. Vicente Miranda, D. Mielenz, J. Klucken, J. Winkler, and W. Xiang. 2019. Extracellular aggregated alpha synuclein primarily triggers lysosomal dysfunction in neural cells prevented by trehalose. *Sci Rep*. 9:544.
- Hornburg, D., C. Drepper, F. Butter, F. Meissner, M. Sendtner, and M. Mann. 2014. Deep proteomic evaluation of primary and cell line motoneuron disease models delineates major differences in neuronal characteristics. *Mol Cell Proteomics*. 13:3410-3420.
- Hosp, F., S. Gutierrez-Angel, M.H. Schaefer, J. Cox, F. Meissner, M.S. Hipp, F.U. Hartl, R. Klein, I. Dudanova, and M. Mann. 2017. Spatiotemporal Proteomic Profiling of Huntington's Disease Inclusions Reveals Widespread Loss of Protein Function. *Cell Rep*. 21:2291-2303.
- Hosp, F., H. Vossfeldt, M. Heinig, D. Vasiljevic, A. Arumughan, E. Wyler, Genetic, G.C. Environmental Risk for Alzheimer's Disease, M. Landthaler, N. Hubner, E.E. Wanker, L. Lannfelt, M. Ingelsson, M. Lalowski, A. Voigt, and M. Selbach. 2015. Quantitative interaction proteomics of neurodegenerative disease proteins. *Cell Rep*. 11:1134-1146.
- Hrabe, T., Y. Chen, S. Pfeffer, L. Kuhn Cuellar, A.-V. Mangold, and F. Förster. 2012. PyTom: A python-based toolbox for localization of macromolecules in cryo-electron tomograms and subtomogram analysis. *Journal of structural biology*. 178:177-188.
- Jiang, M., and G. Chen. 2006. High Ca²⁺-phosphate transfection efficiency in low-density neuronal cultures. *Nat Protoc*. 1:695-700.
- Jo, C., S. Gundemir, S. Pritchard, Y.N. Jin, I. Rahman, and G.V. Johnson. 2014. Nrf2 reduces levels of phosphorylated tau protein by inducing autophagy adaptor protein NDP52. *Nat Commun*. 5:3496.

- Khatter, H., A.G. Myasnikov, S.K. Natchiar, and B.P. Klaholz. 2015. Structure of the human 80S ribosome. *Nature*. 520:640-645.
- Kim, Y.E., F. Hosp, F. Frottin, H. Ge, M. Mann, M. Hayer-Hartl, and F.U. Hartl. 2016. Soluble Oligomers of PolyQ-Expanded Huntingtin Target a Multiplicity of Key Cellular Factors. *Mol Cell*. 63:951-964.
- Klucken, J., A.M. Poehler, D. Ebrahimi-Fakhari, J. Schneider, S. Nuber, E. Rockenstein, U. Schlotzer-Schrehardt, B.T. Hyman, P.J. McLean, E. Masliah, and J. Winkler. 2012. Alpha-synuclein aggregation involves a bafilomycin A 1-sensitive autophagy pathway. *Autophagy*. 8:754-766.
- Kremer, J.R., D.N. Mastronarde, and J.R. McIntosh. 1996. Computer visualization of three-dimensional image data using IMOD. *J Struct Biol*. 116:71-76.
- Lamark, T., and T. Johansen. 2012. Aggrephagy: selective disposal of protein aggregates by macroautophagy. *Int J Cell Biol*. 2012:736905.
- Li, X., P. Mooney, S. Zheng, C.R. Booth, M.B. Braunfeld, S. Gubbens, D.A. Agard, and Y. Cheng. 2013. Electron counting and beam-induced motion correction enable near-atomic-resolution single-particle cryo-EM. *Nat Methods*. 10:584-590.
- Louis, J.V., E. Martens, P. Borghgraef, C. Lambrecht, W. Sents, S. Longin, K. Zwaenepoel, R. Pijnenborg, I. Landrieu, G. Lippens, B. Ledermann, J. Gotz, F. Van Leuven, J. Goris, and V. Janssens. 2011. Mice lacking phosphatase PP2A subunit PR61/B'delta (Ppp2r5d) develop spatially restricted tauopathy by deregulation of CDK5 and GSK3beta. *Proc Natl Acad Sci U S A*. 108:6957-6962.
- Martinez-Sanchez, A., I. Garcia, S. Asano, V. Lucic, and J.J. Fernandez. 2014. Robust membrane detection based on tensor voting for electron tomography. *J Struct Biol*. 186:49-61.
- Mastronarde, D.N. 2005. Automated electron microscope tomography using robust prediction of specimen movements. *J Struct Biol*. 152:36-51.
- Mauvezin, C., P. Nagy, G. Juhasz, and T.P. Neufeld. 2015. Autophagosome-lysosome fusion is independent of V-ATPase-mediated acidification. *Nat Commun*. 6:7007.
- May, S., D. Hornburg, M.H. Schludi, T. Arzberger, K. Rentzsch, B.M. Schwenk, F.A. Grasser, K. Mori, E. Kremmer, J. Banzhaf-Strathmann, M. Mann, F. Meissner, and D. Edbauer. 2014. C9orf72 FTL/ALS-associated Gly-Ala dipeptide repeat proteins cause neuronal toxicity and Unc119 sequestration. *Acta Neuropathol*. 128:485-503.
- Mazzulli, J.R., Y.H. Xu, Y. Sun, A.L. Knight, P.J. McLean, G.A. Caldwell, E. Sidransky, G.A. Grabowski, and D. Krainc. 2011. Gaucher disease glucocerebrosidase and alpha-synuclein form a bidirectional pathogenic loop in synucleinopathies. *Cell*. 146:37-52.
- Mazzulli, J.R., F. Zunke, O. Isacson, L. Studer, and D. Krainc. 2016. alpha-Synuclein-induced lysosomal dysfunction occurs through disruptions in protein trafficking in human midbrain synucleinopathy models. *Proc Natl Acad Sci U S A*. 113:1931-1936.
- Menzies, F.M., A. Fleming, and D.C. Rubinsztein. 2015. Compromised autophagy and neurodegenerative diseases. *Nat Rev Neurosci*. 16:345-357.
- Newell-Litwa, K., E. Seong, M. Burmeister, and V. Faundez. 2007. Neuronal and non-neuronal functions of the AP-3 sorting machinery. *J Cell Sci*. 120:531-541.
- Ohno, H., R.C. Aguilar, D. Yeh, D. Taura, T. Saito, and J.S. Bonifacino. 1998. The medium subunits of adaptor complexes recognize distinct but overlapping sets of tyrosine-based sorting signals. *J Biol Chem*. 273:25915-25921.
- Olsen, J.V., B. Macek, O. Lange, A. Makarov, S. Horning, and M. Mann. 2007. Higher-energy C-trap dissociation for peptide modification analysis. *Nat Methods*. 4:709-712.
- Olzscha, H., S.M. Schermann, A.C. Woerner, S. Pinkert, M.H. Hecht, G.G. Tartaglia, M. Vendruscolo, M. Hayer-Hartl, F.U. Hartl, and R.M. Vabulas. 2011. Amyloid-like aggregates sequester numerous metastable proteins with essential cellular functions. *Cell*. 144:67-78.
- Peden, A.A., R.E. Rudge, W.W. Lui, and M.S. Robinson. 2002. Assembly and function of AP-3 complexes in cells expressing mutant subunits. *J Cell Biol*. 156:327-336.
- Platt, F.M., A. d'Azzo, B.L. Davidson, E.F. Neufeld, and C.J. Tiffit. 2018. Lysosomal storage diseases. *Nat Rev Dis Primers*. 4:27.

- Raimundo, N., S. Vanharanta, L.A. Aaltonen, I. Hovatta, and A. Suomalainen. 2009. Downregulation of SRF-FOS-JUNB pathway in fumarate hydratase deficiency and in uterine leiomyomas. *Oncogene*. 28:1261-1273.
- Rigort, A., F.J. Bauerlein, A. Leis, M. Gruska, C. Hoffmann, T. Laugks, U. Bohm, M. Eibauer, H. Gnaegi, W. Baumeister, and J.M. Plitzko. 2010. Micromachining tools and correlative approaches for cellular cryo-electron tomography. *J Struct Biol*. 172:169-179.
- Rigort, A., F.J. Bauerlein, E. Villa, M. Eibauer, T. Laugks, W. Baumeister, and J.M. Plitzko. 2012. Focused ion beam micromachining of eukaryotic cells for cryoelectron tomography. *Proc Natl Acad Sci U S A*. 109:4449-4454.
- Robak, L.A., I.E. Jansen, J. van Rooij, A.G. Uitterlinden, R. Kraaij, J. Jankovic, C. International Parkinson's Disease Genomics, P. Heutink, and J.M. Shulman. 2017. Excessive burden of lysosomal storage disorder gene variants in Parkinson's disease. *Brain*. 140:3191-3203.
- Rovelet-Lecrux, A., C. Charbonnier, D. Wallon, G. Nicolas, M.N. Seaman, C. Pottier, S.Y. Breusegem, P.P. Mathur, P. Jenardhanan, K. Le Guennec, A.S. Mukadam, O. Quenez, S. Coutant, S. Rousseau, A.C. Richard, A. Boland, J.F. Deleuze, T. Frebourg, D. Hannequin, D. Campion, and C.-M. collaborators. 2015. De novo deleterious genetic variations target a biological network centered on Abeta peptide in early-onset Alzheimer disease. *Mol Psychiatry*. 20:1046-1056.
- Ruepp, A., B. Waegle, M. Lechner, B. Brauner, I. Dunger-Kaltenbach, G. Fobo, G. Frishman, C. Montrone, and H.W. Mewes. 2010. CORUM: the comprehensive resource of mammalian protein complexes--2009. *Nucleic Acids Res*. 38:D497-501.
- Sardiello, M., M. Palmieri, A. di Ronza, D.L. Medina, M. Valenza, V.A. Gennarino, C. Di Malta, F. Donaudy, V. Embrione, R.S. Polishchuk, S. Banfi, G. Parenti, E. Cattaneo, and A. Ballabio. 2009. A gene network regulating lysosomal biogenesis and function. *Science*. 325:473-477.
- Saudou, F., and S. Humbert. 2016. The Biology of Huntingtin. *Neuron*. 89:910-926.
- Schindelin, J., I. Arganda-Carreras, E. Frise, V. Kaynig, M. Longair, T. Pietzsch, S. Preibisch, C. Rueden, S. Saalfeld, B. Schmid, J.Y. Tinevez, D.J. White, V. Hartenstein, K. Eliceiri, P. Tomancak, and A. Cardona. 2012. Fiji: an open-source platform for biological-image analysis. *Nat Methods*. 9:676-682.
- Settembre, C., C. Di Malta, V.A. Polito, M. Garcia Arencibia, F. Vetrini, S. Erdin, S.U. Erdin, T. Huynh, D. Medina, P. Colella, M. Sardiello, D.C. Rubinsztein, and A. Ballabio. 2011. TFEB links autophagy to lysosomal biogenesis. *Science*. 332:1429-1433.
- Settembre, C., A. Fraldi, D.L. Medina, and A. Ballabio. 2013. Signals from the lysosome: a control centre for cellular clearance and energy metabolism. *Nat Rev Mol Cell Biol*. 14:283-296.
- Shirasaki, D.I., E.R. Greiner, I. Al-Ramahi, M. Gray, P. Boontheung, D.H. Geschwind, J. Botas, G. Coppola, S. Horvath, J.A. Loo, and X.W. Yang. 2012. Network organization of the huntingtin proteomic interactome in mammalian brain. *Neuron*. 75:41-57.
- Soto, C., and S. Pritzkow. 2018. Protein misfolding, aggregation, and conformational strains in neurodegenerative diseases. *Nature neuroscience*. 21:1332-1340.
- Suzuki, K., and R.D. Terry. 1967. Fine structural localization of acid phosphatase in senile plaques in Alzheimer's presenile dementia. *Acta Neuropathol*. 8:276-284.
- Taylor, J.P., R.H. Brown, Jr., and D.W. Cleveland. 2016. Decoding ALS: from genes to mechanism. *Nature*. 539:197-206.
- Usenovic, M., E. Tresse, J.R. Mazzulli, J.P. Taylor, and D. Krainc. 2012. Deficiency of ATP13A2 leads to lysosomal dysfunction, alpha-synuclein accumulation, and neurotoxicity. *J Neurosci*. 32:4240-4246.
- Vincenz-Donnelly, L., H. Holthausen, R. Korner, E.C. Hansen, J. Presto, J. Johansson, R. Sawarkar, F.U. Hartl, and M.S. Hipp. 2018. High capacity of the endoplasmic reticulum to prevent secretion and aggregation of amyloidogenic proteins. *EMBO J*. 37:337-350.
- Wagner, J., M. Schaffer, and R. Fernandez-Busnadiego. 2017. Cryo-electron tomography-the cell biology that came in from the cold. *FEBS Lett*. 591:2520-2533.
- Wang, C., M.A. Telpoukhovskaia, B.A. Bahr, X. Chen, and L. Gan. 2018. Endo-lysosomal dysfunction: a converging mechanism in neurodegenerative diseases. *Curr Opin Neurobiol*. 48:52-58.

- West, M.W., W. Wang, J. Patterson, J.D. Mancias, J.R. Beasley, and M.H. Hecht. 1999. De novo amyloid proteins from designed combinatorial libraries. *Proc Natl Acad Sci U S A*. 96:11211-11216.
- Winder-Rhodes, S.E., P. Garcia-Reitböck, M. Ban, J.R. Evans, T.S. Jacques, A. Kemppinen, T. Foltynie, C.H. Williams-Gray, P.F. Chinnery, G. Hudson, D.J. Burn, L.M. Allcock, S.J. Sawcer, R.A. Barker, and M.G. Spillantini. 2012. Genetic and pathological links between Parkinson's disease and the lysosomal disorder Sanfilippo syndrome. *Mov Disord*. 27:312-315.
- Winklhofer, K.F., J. Tatzelt, and C. Haass. 2008. The two faces of protein misfolding: gain- and loss-of-function in neurodegenerative diseases. *EMBO J*. 27:336-349.
- Winner, B., R. Jappelli, S.K. Maji, P.A. Desplats, L. Boyer, S. Aigner, C. Hetzer, T. Loher, M. Vilar, S. Campioni, C. Tzitzilonis, A. Soragni, S. Jessberger, H. Mira, A. Consiglio, E. Pham, E. Masliah, F.H. Gage, and R. Riek. 2011. In vivo demonstration that alpha-synuclein oligomers are toxic. *Proc Natl Acad Sci U S A*. 108:4194-4199.
- Winslow, A.R., C.W. Chen, S. Corrochano, A. Acevedo-Arozena, D.E. Gordon, A.A. Peden, M. Lichtenberg, F.M. Menzies, B. Ravikumar, S. Imarisio, S. Brown, C.J. O'Kane, and D.C. Rubinsztein. 2010. alpha-Synuclein impairs macroautophagy: implications for Parkinson's disease. *J Cell Biol*. 190:1023-1037.
- Woerner, A.C., F. Frottin, D. Hornburg, L.R. Feng, F. Meissner, M. Patra, J. Tatzelt, M. Mann, K.F. Winklhofer, F.U. Hartl, and M.S. Hipp. 2016. Cytoplasmic protein aggregates interfere with nucleocytoplasmic transport of protein and RNA. *Science*. 351:173-176.
- Wong, Y.C., and E.L. Holzbaur. 2014. The regulation of autophagosome dynamics by huntingtin and HAP1 is disrupted by expression of mutant huntingtin, leading to defective cargo degradation. *J Neurosci*. 34:1293-1305.
- Yamamoto, A., and Z. Yue. 2014. Autophagy and its normal and pathogenic states in the brain. *Annu Rev Neurosci*. 37:55-78.
- Yang, H., and H.Y. Hu. 2016. Sequestration of cellular interacting partners by protein aggregates: implication in a loss-of-function pathology. *The FEBS journal*. 283:3705-3717.
- Zhou, C., B.D. Slaughter, J.R. Unruh, F. Guo, Z. Yu, K. Mickey, A. Narkar, R.T. Ross, M. McClain, and R. Li. 2014. Organelle-based aggregation and retention of damaged proteins in asymmetrically dividing cells. *Cell*. 159:530-542.

Figure legends

Figure 1. β proteins aggregate and cause toxicity in transfected primary neurons. **a**, Transfected cortical neurons at DIV 10+1. Arrows point to β protein aggregates. **b**, Percentage of transfected neurons bearing aggregates at DIV 10+1 (n=3 independent experiments, 25-45 cells/condition/experiment; One-way ANOVA with Dunnett's post hoc test). **c**, Examples of DIV10+1 β 23-mCherry neurons positive (top) and negative (bottom) for cleaved caspase-3. **d**, Percentage of transfected neurons positive for cleaved caspase-3 (n=3 independent experiments, 25-45 cells/condition/experiment; Two-way ANOVA with Tukey's post hoc test). **e**, Examples of primary hippocampal neurons transfected with mCherry or β 23-mCherry at DIV 10+2. Images are colour-inverted with mCherry fluorescence shown in black. Note that the β 23-mCherry cell has fewer primary dendrites. **f**, Sholl analysis reveals reduced dendritic complexity in the presence of β proteins (n=3

independent experiments, 10-30 cells/condition/experiment; Two-way ANOVA with Tukey's post hoc test). * $p < 0.05$; *** $p < 0.001$; **** $p < 0.0001$. Scale bars, 5 μm in **a** and **c**; 50 μm in **e**.

Figure 2. Ultrastructure of β protein aggregates in primary neurons. **a**, Tomographic slice of a β 4-mCherry aggregate in a transfected DIV 6+1 cortical neuron. The area marked by the box is magnified in the inset. Red arrowheads point to β 4-mCherry fibrils. Agg, β 4-mCherry aggregate; En, endosome; ER, endoplasmic reticulum; Mit, mitochondrion. **b**, 3D rendering of the tomogram shown in **a**. β 4-mCherry fibrils, blue; mitochondria, green; ER membranes, salmon; endosome, gold; vesicles, cyan; ribosomes, yellow; microtubules, brown. Scale bars in **a**, 200 nm and 50 nm (inset).

Figure 3. Aberrant lysosomal ultrastructure in β protein-expressing neurons. **a**, Example of a lysosome in a tomogram from a DIV 6+1 cortical neuron transfected with mCherry. **c**, Example of a lysosome in a neuron transfected with β 4-mCherry. Note the presence of abundant membrane stacks and electron-dense material within the lysosome. En, endosome; ER, endoplasmic reticulum; LE, late endosome; Lys, lysosome; Mit, mitochondrion; PM, plasma membrane. **b**, **d**, 3D rendering of the tomograms shown in **a** and **c**, respectively. Lysosomal membrane, purple; membrane stacks within the lysosomes, green; intraluminal vesicles, gold; other cellular membranes, grey. For additional examples see Supplementary Fig. S4. Scale bars in **a** and **c**, 200 nm.

Figure 4. Defects of lysosomal morphology and function in the presence of β proteins. **a**, Fluorescent images of DIV 6+1 primary cortical neurons transfected with mCherry (top) or β 4-mCherry (bottom) and incubated with LysoTracker Green. White dashed lines show the contours of the neuron. Yellow circles outline lysosomes. **b**, Distribution of the lysosomal size in control and β protein-expressing neurons (mCherry, $n=2148$ lysosomes from 36 cells; β 4-mCherry, $n=1595$ lysosomes from 44 cells; β 23-mCherry, $n=1838$ lysosomes from 46 cells; from 4 independent experiments; Two-tailed Mann-Whitney test). **c**, Box plot showing the number of lysosomes per neuron (mCherry, $n=36$ cells; β 4-mCherry, $n=44$ cells; β 23-mCherry, $n=46$ cells; from 4 independent experiments; Two-tailed Mann-Whitney test). **d**, Western blots for autophagy markers in lysates of HeLa cells transfected with mCherry or β 23-mCherry. HPRT was used as a loading control. **e**, Western blot quantification ($n=5$ independent experiments; Two-tailed t-test). **f**, Transcript levels of

lysosomal genes in mCherry or β 23-mCherry HeLa cells determined with RT-PCR (n=6 experiments; Two-tailed t-test). **g**, Quantification of neurons with fragmented nuclei in DIV 6+1 cortical cultures transfected with the indicated constructs and treated or not treated with 80 nM Bafilomycin A1 (n=3 independent experiments, 20-130 cells/condition/experiment; Two-way ANOVA with Sidak's post hoc test). *p<0.05; **p<0.01; ***p<0.001. Scale bars in **a**, 10 μ m.

Figure 5. β protein interactome in primary neurons. **a**, Venn diagram depicting numbers and overlap of interactors for the three β proteins investigated. **b-d**, Volcano plots depicting proteins significantly enriched in β protein IPs. Red dots denote proteins that pass 5% permutation-based FDR (curved line on the right; proteins significantly associated with mCherry are not highlighted for the interactomes). **e**, Heat map of common interactors of all three β proteins. **f-h**, Pie charts showing the quantitative composition of β protein-interacting complex.

Figure 6. AP-3 μ 1 overexpression ameliorates β protein-dependent toxicity. **a**, Single confocal plane images of DIV 6+1 cortical neurons co-transfected with AP-3 μ 1 and either mCherry (top) or β 23-mCherry (bottom). The areas marked by the boxes are magnified in the insets. **b**, Quantification of Person's correlation coefficient between the AP-3 μ 1 and mCherry or AP-3 μ 1 and β protein signal (n=3 independent experiments, 10-30 cells/condition/experiment; One-way ANOVA with Tukey's post hoc test). **c**, Examples of cleaved caspase-3 staining in DIV 6+1 cortical neurons co-transfected with β 23-mCherry and either EGFP (top) or AP-3 μ 1 (bottom). **d**, Percentage of double-transfected neurons positive for cleaved caspase-3 (n=3 independent experiments; 10-60 cells/condition/experiment; Two-tailed t-test). Anti-Flag staining was used to detect AP-3 μ 1 in **a**, **c**. *p<0.05; ***p<0.001. Scale bars, 10 μ m in **a**; 50 μ m in **c**.

Supplementary figure legends

Supplementary Figure S1. Lentiviral transduction of β proteins leads to aggregation and toxicity in primary neurons. **a**, Primary cortical neurons transduced with mCherry or with β proteins at indicated time points. Transduced proteins were visualized by myc staining. Insets show examples of β protein aggregates. **b**, Quantification of neuronal survival determined by MTT assay at the indicated time points (n=4 independent experiments; Two-way ANOVA with Tukey's post hoc test). **c**,

Western blot showing expression of mCherry and β proteins in lentivirally transduced neurons at DIV 10+3. Tubulin was used as a loading control. Two lanes on the blot between β 4-mCherry and β 23-mCherry were digitally removed. **d**, Quantification of expression levels of mCherry, β 4-mCherry and β 23-mCherry proteins (n=4 Western blots from independent cultures; One-way ANOVA with Dunnett's post hoc test). *p<0.05; ***p<0.001; ****p<0.0001; n.s. – not significant. Scale bar in **a**, 5 μ m.

Supplementary Figure S2. Cryo-electron tomography sample preparation workflow. **a**, Vitrified cells on EM grids are imaged by cryo-light microscopy and cells of interest are identified. **b**, Grids are transferred to a cryo-FIB / scanning electron microscope (SEM) and positions of cells of interest are found via cryo-light microscopy (LM) / cryo-SEM correlation. **c-d**, Cells are thinned to a thickness of max. 200 nm by means of FIB milling. **e**, Grids are transferred to a cryo-transmission electron microscope (TEM) and regions of interest are identified via cryo-LM / cryo-TEM correlation and **f**, imaged by cryo-electron tomography. IC, ice contamination; Pt, platinum coating. Scale bars in **a**, 500 μ m; **b**, 50 μ m; **c** and **d**, 10 μ m; **e**, 3 μ m; **f**, 200 nm.

Supplementary Figure S3. Comparable aggregate morphology and cellular interactions in neurons and HeLa cells. Tomograms of β 23-mCherry aggregates in primary neurons (**a**) and HeLa cells (**c**). Red arrowheads point to β 23 fibrils (insets). White arrowheads point to intracellular membranes (lower insets). Agg, β protein aggregate; En, endosome; ER, endoplasmic reticulum; Lys, lysosome; Mit, mitochondrion. **b**, **d**, 3D rendering of the tomograms shown in **a** and **c**, respectively. ER membranes are found in close proximity to both aggregates and mitochondrial and lysosomal membranes. Black arrows indicate ER - mitochondria contact sites. β 23-mCherry fibrils, blue; mitochondria, green; ER membranes, salmon; endosomes, gold; lysosomes, purple; vesicles, cyan; microtubules, brown. Scale bars in **a** and **c**, 200 nm and 50 nm (insets).

Supplementary Figure S4. Gallery of lysosomal morphologies. Tomograms from neurons transfected with mCherry (**a-c**) and β 4-mCherry (**d-f**). Note that in cells with β protein aggregates, lysosomes often contain extensive stacks of membranes (**d-f**). Inset in **e** shows an example of an early autophagosome. Agg, β protein aggregate; AS, autophagosome; En, endosome; ER,

endoplasmic reticulum; LD, lipid droplet; LE, late endosome; Lys, lysosome; Mit, mitochondrion; PM, plasma membrane. Scale bars in **a-f**, 200 nm; inset in **e**, 100 nm.

Supplementary Figure S5. GO annotations and bioinformatic characterization of β protein interactors. **a-c**, Pathway enrichment analysis of interactors of β 4-mCherry (**a**), β 17-mCherry (**b**) and β 23-mCherry (**c**). **d**, Box plots of LCR content in all identified proteins and in β protein interactors (n=4 independent experiments; Two-sample Wilcoxon test). **p<0.01; ****p<0.0001; n.s. – not significant.

Supplementary Figure S6. Total proteome of β protein-expressing neurons. **a**, Numbers of identified proteins in all conditions together, and in neurons transduced with the indicated constructs (n=4 independent experiments). **b-d**, Volcano plots of the total proteome of β protein compared to mCherry neurons. Significantly regulated proteins are shown in red; Interactors of the respective β protein in black; AP-3 μ 1 is highlighted in green. **e**, Abundance ranking of all identified proteins. AP-3 μ 1 (indicated in blue) is at position 1,296.

Supplementary Tables

Supplementary Table S1. β protein interactors and proteins significantly changed in the total proteome.

Supplementary Table S2. Total proteome of primary neurons expressing β proteins.

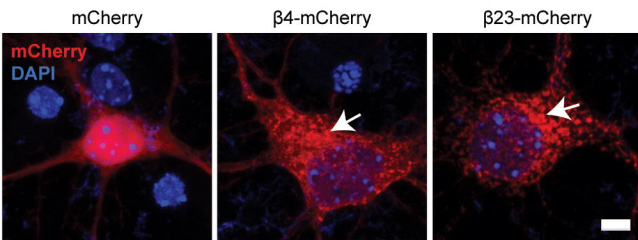
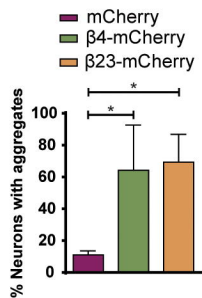
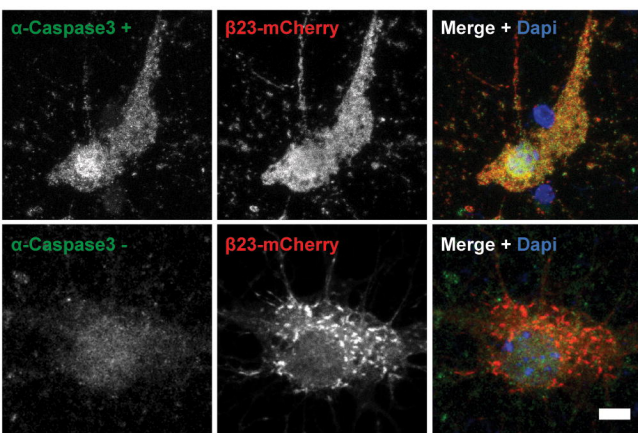
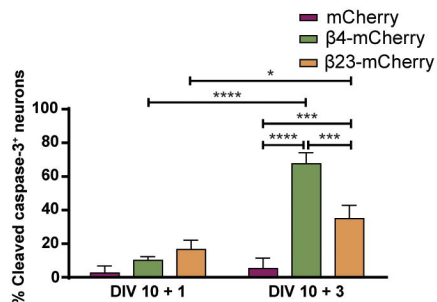
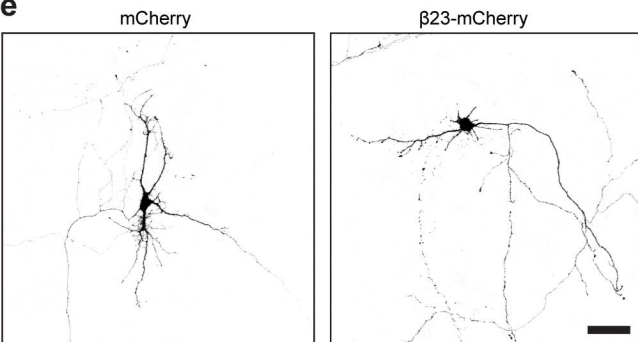
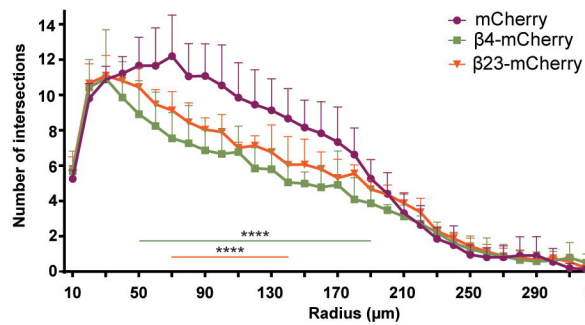
Figure 1**a****b****c****d****e****f**

Figure 3

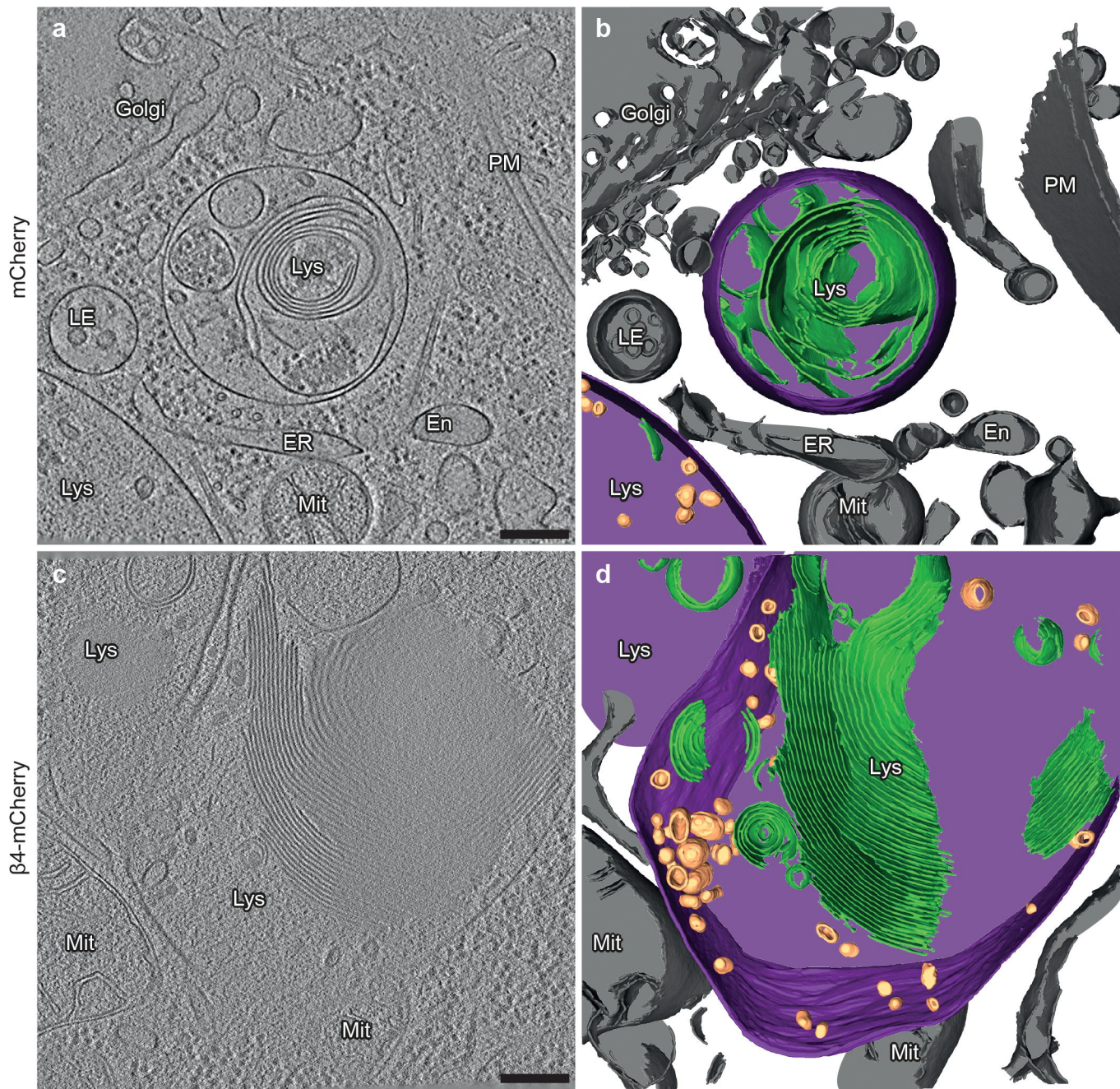


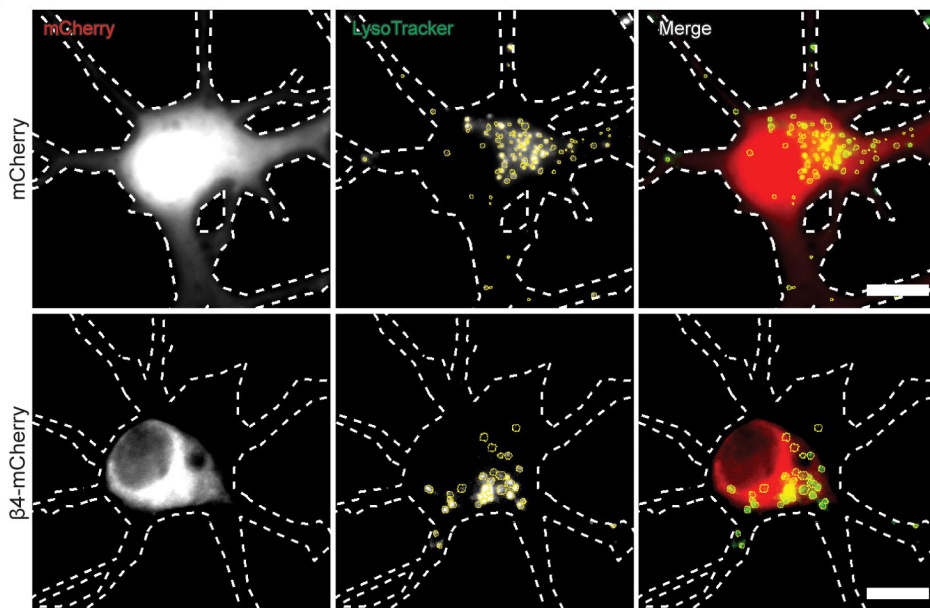
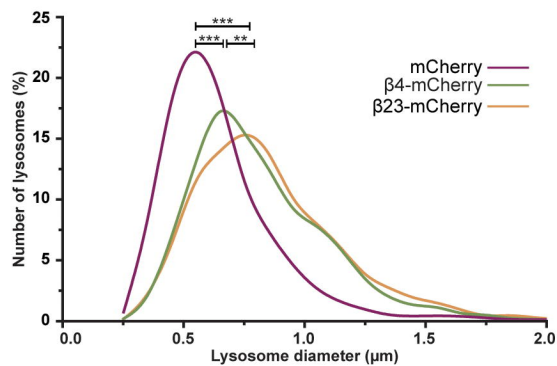
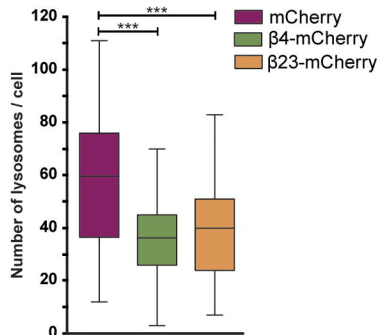
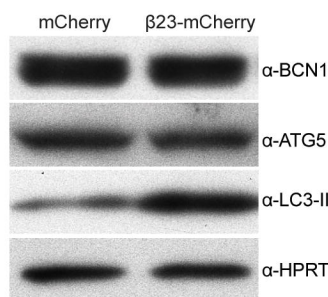
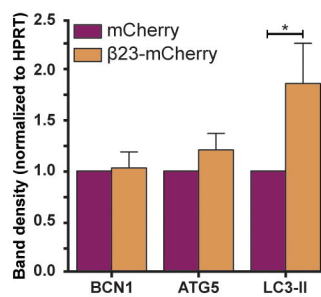
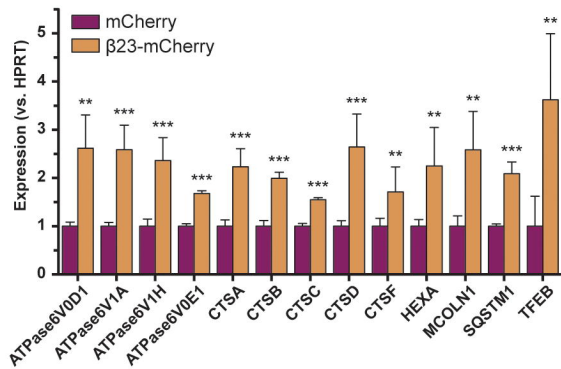
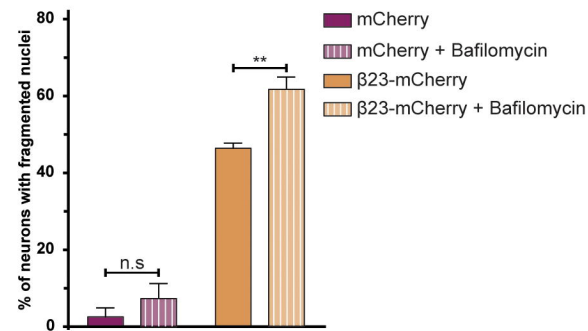
Figure 4**a****b****c****d****e****f****g**

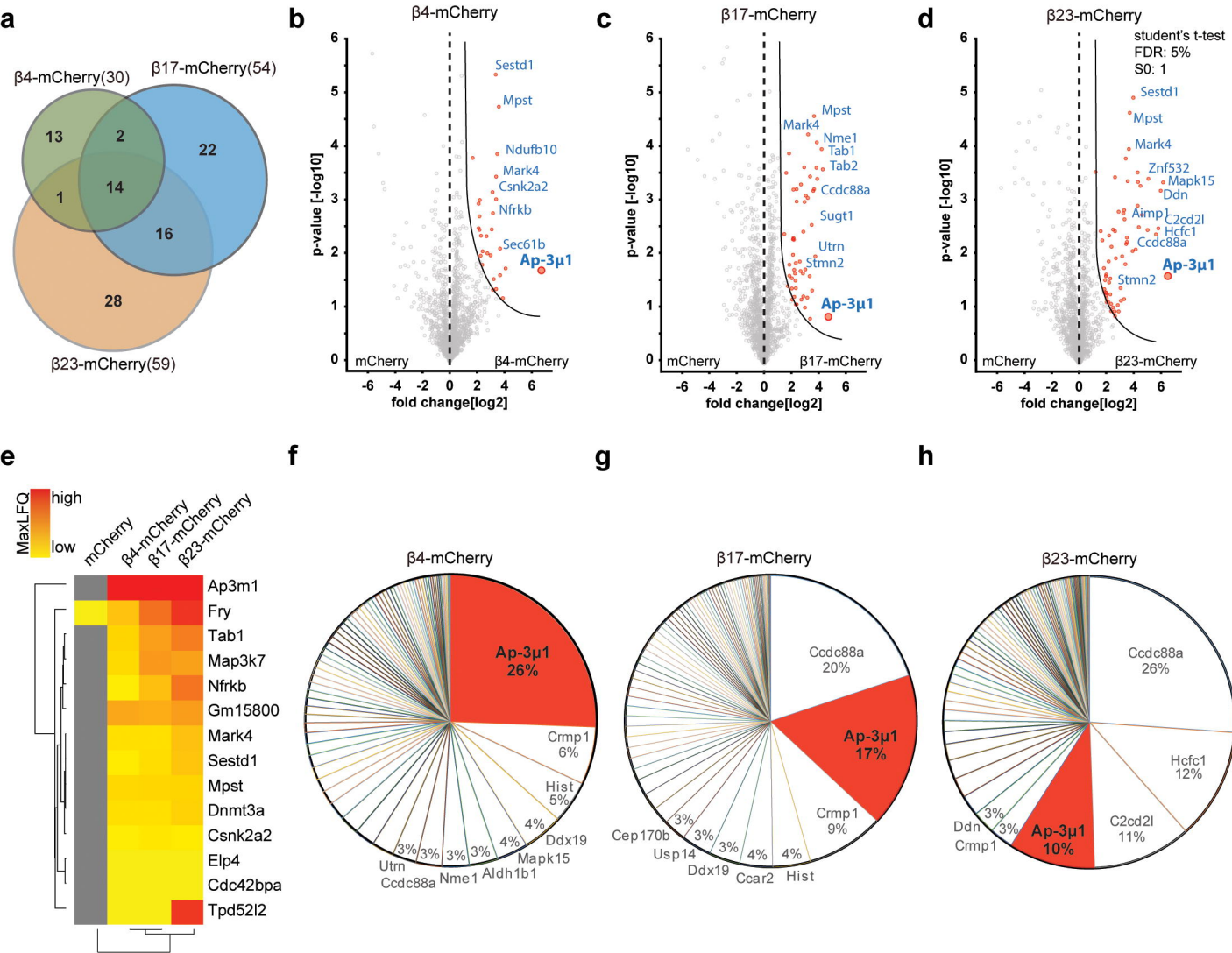
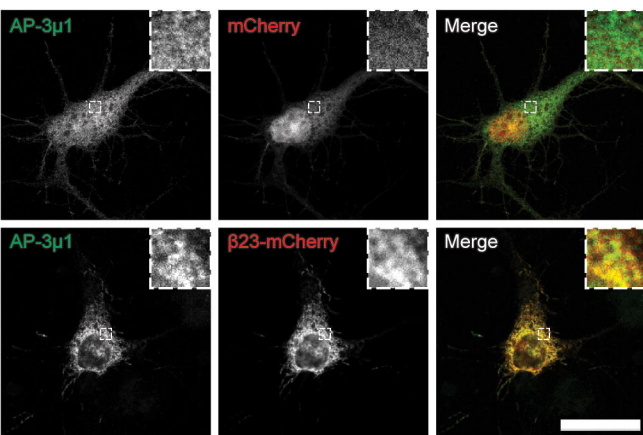
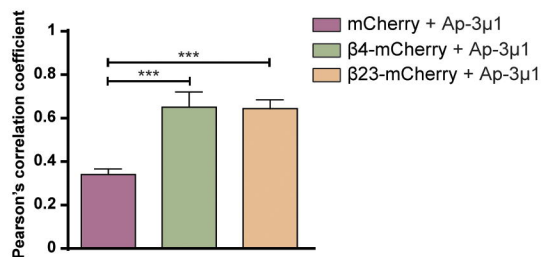
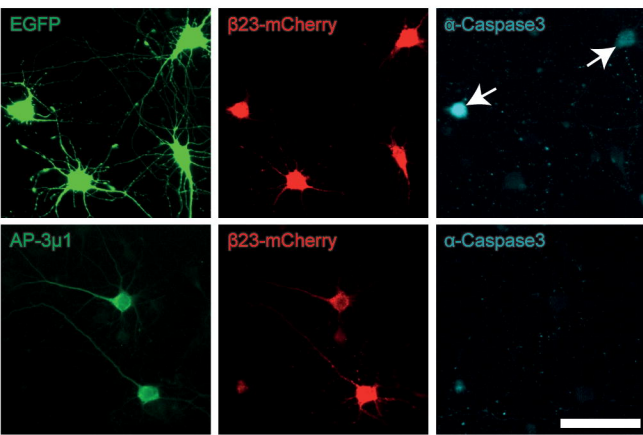
Figure 5

Figure 6**a****b****c****d**